

# Calcium and titanium isotopic fractionations during evaporation

Junjun Zhang<sup>a,\*</sup>, Shichun Huang<sup>b</sup>, Andrew M. Davis<sup>a</sup>, Nicolas Dauphas<sup>a</sup>,  
Akihiko Hashimoto<sup>c</sup>, Stein B. Jacobsen<sup>d</sup>

<sup>a</sup> *Origins Laboratory, Department of the Geophysical Sciences, Enrico Fermi Institute, and Chicago Center for Cosmochemistry,  
The University of Chicago, 5734 South Ellis Avenue, Chicago, IL 60637, USA*

<sup>b</sup> *Department of Geoscience, University of Nevada, 4505 S. Maryland Parkway, Las Vegas, NV 89154, USA*

<sup>c</sup> *Department of Cosmosciences, Hokkaido University, Science Bldg. #8, Kita-10, Nishi-8, Sapporo 060-0810, Japan*

<sup>d</sup> *Department of Earth and Planetary Sciences, Harvard University, 20 Oxford Street, Cambridge, MA 02138, USA*

Received 20 September 2012; accepted in revised form 15 May 2014; Available online 9 June 2014

## Abstract

Isotope fractionations associated with high temperature evaporation provide important constraints on the physicochemical processes that affected planetary materials at the birth of the solar system. Previous evaporation experiments have focused on isotopic fractionation of moderately to highly volatile elements. Here, we investigate the isotope fractionation behavior of two highly refractory elements, calcium and titanium, during evaporation of perovskite ( $\text{CaTiO}_3$ ) in a vacuum furnace. In our experiments, isotope fractionation during evaporation follows the Rayleigh law, but not the commonly used exponential law, with the dominant evaporating species being  $\text{Ca}_{(g)}$  and  $\text{TiO}_{2(g)}$ . If isotope fractionations in early solar system materials did follow the Rayleigh law, the common practice of using an exponential fractionation law to correct for mass-dependent fractionation in the study of mass-independent fractionations may introduce significant artificial isotope anomalies.

© 2014 Elsevier Ltd. All rights reserved.

## 1. INTRODUCTION

Materials in our solar system display both mass-dependent isotope fractionations (MDFs) and mass-independent fractionations (MIFs, or isotope anomalies). MDFs can be produced by various processes, including equilibrium partitioning between phases, diffusion, and evaporation/condensation. Isotope anomalies are departures from the laws of MDF and can be ascribed to mass-independent processes, such as radioactive decay, nuclear transmutations induced by exposure to cosmic rays, photochemical reactions, or inheritance of nucleosynthetic effects. Determining isotope variations including both MDFs and isotope anomalies

can help to understand what processes shaped the chemical composition of solar system materials, and to unravel their origins. While isotope anomalies of refractory elements have been extensively studied in early solar system materials (e.g., Dauphas et al., 2002; Birck, 2004; and references therein), MDFs for refractory elements have been explored to a lesser extent. Previous studies on evaporation-driven MDFs focused on the moderately to highly volatile elements oxygen, magnesium, silicon, potassium, iron, cadmium, and mercury (Esat et al., 1986; Molini-Velsko et al., 1987; Davis et al., 1990; Wang et al., 1994, 1999, 2001; Grossman et al., 2000; Richter et al., 2002; Yu et al., 2003; Dauphas et al., 2004; Wombacher et al., 2004; Yamada et al., 2006; Tachibana et al., 2007; Richter et al., 2007, 2011; Estrade et al., 2009; Knight et al., 2009). Evaporation-driven MDFs of refractory elements calcium and titanium have only been explored preliminarily using an ion probe (Davis et al., 1995).

\* Corresponding author. Present address: Department of Civil & Environmental Engineering, Hong Kong Polytechnic University, Hung Hom, Kowloon, Hong Kong.

E-mail address: [jjzhang@polyu.edu.hk](mailto:jjzhang@polyu.edu.hk) (J. Zhang).

Refractory calcium, aluminium-rich inclusions (CAIs), the oldest known solar system objects (Dauphas and Chaussidon, 2011; MacPherson, 2014; Davis and McKeegan, 2014, and references therein), are highly enriched in calcium and titanium compared to average chondritic composition. Significant MDFs of calcium and titanium were found for some CAIs, up to 12.9‰ amu<sup>-1</sup> and 19.0‰ amu<sup>-1</sup>, respectively (Niederer et al., 1985; Clayton et al., 1988; Ireland, 1990; Ireland et al., 1992), which may result from high temperature evaporation–condensation processes (e.g., Niederer et al., 1985; Clayton et al., 1988; Huang et al., 2012). However, a quantitative understanding has been lacking because critical parameters needed to model these processes were missing.

In the past few decades, isotope anomalies of calcium and titanium in CAIs have been extensively studied to provide insights into the nucleosynthetic origin of neutron-rich isotopes in the calcium–titanium mass region and to characterize the degree of isotope heterogeneity in the early Solar System (e.g., Niederer and Papanastassiou, 1984; Niederer et al., 1985; Leya et al., 2009; Simon et al., 2009; Trinquier et al., 2009; Moynier et al., 2010; Chen et al., 2011; Huang et al., 2012). In these MIF studies, the exponential MDF law has been used to correct for both naturally occurring and instrumental MDF. It has been shown that instrumental fractionation of calcium with thermal ionization mass spectrometry (TIMS) or zinc with multicollector-inductively coupled plasma mass spectrometer (MC-ICPMS) follows an exponential law (Russell et al., 1978; Hart and Zindler, 1989; Maréchal et al., 1999), and this law has also been used for both TIMS measurements and MC-ICPMS measurements of titanium isotopes. However, the natural fractionations of calcium and titanium may not follow the exponential law.

In this paper, we investigated the fundamental properties of calcium and titanium MDFs during evaporation of CaTiO<sub>3</sub>. Equilibrium thermodynamic calculations predict that the dominant evaporating species of calcium and titanium from CaO–TiO<sub>2</sub> are Ca atoms and TiO<sub>2</sub> molecules. We found that both calcium and titanium evaporation MDFs follow the Rayleigh law with the masses of the thermodynamically dominant species, but not the widely used exponential law. Our results allow us to examine the validity of previous isotope anomaly studies where the exponential MDF law had been used.

## 2. THEORETICAL FRAMEWORK

### 2.1. Isotope fractionation factor

The distribution of two stable isotopes *i* and *k* between two phases is controlled by equilibrium and kinetic factors. During high temperature evaporation, the net flux of an isotope *i* from a condensed phase to a surrounding gas is equal to the difference between the evaporation flux and the condensation flux. It is given by Hertz–Knudsen equation (Hirth and Pound, 1963):

$$J_i = J_{i, \text{evap}} - J_{i, \text{cond}} = n_i \gamma_i \frac{(P_{i, \text{sat}} - P_i)}{\sqrt{2\pi m_i RT}} \quad (1)$$

where  $J_i$ ,  $J_{i, \text{evap}}$ , and  $J_{i, \text{cond}}$  are the net flux, evaporation flux, and condensation flux of *i* in moles per unit area per unit time, respectively,  $n_i$  is the number of atoms of *i* in the gas species molecule,  $\gamma_i$  is the evaporation (or condensation) coefficient of *i*,  $P_{i, \text{sat}}$  is the saturation vapor pressure of *i*,  $P_i$  is the partial pressure of *i* striking the surface of the condensed phase,  $m_i$  is the molar mass of gas species containing *i*,  $R$  is the gas constant, and  $T$  is the absolute temperature.

In our study, we consider free evaporation (i.e., kinetic evaporation into vacuum;  $P_i = 0$ ; condensation flux  $J_{i, \text{cond}} = 0$ ) and the dominant evaporating species for calcium and titanium are assumed to be Ca and TiO<sub>2</sub>, respectively (i.e.,  $n_i = 1$ ; see Section 5.1). Equation (1) then becomes

$$J_i = \frac{\gamma_i R_{i, \text{sat}}}{\sqrt{2\pi m_i RT}} \quad (2)$$

The ratio of two isotopes *i* and *k* in the gas phase  $R_{ik, \text{gas}}$  for free evaporation is

$$R_{ik, \text{gas}} = \frac{J_i}{J_k} = \frac{\gamma_i}{\gamma_k} \frac{P_{i, \text{sat}}}{P_{k, \text{sat}}} \sqrt{\frac{m_k}{m_i}} \quad (3)$$

The fractionation factor  $\alpha_{ik}$  is defined as

$$\alpha_{ik} = \frac{R_{ik, \text{gas}}}{R_{ik, \text{cond}}} = \frac{J_i/J_k}{R_{ik, \text{cond}}} \quad (4)$$

where  $R_{ik, \text{gas}}$  is the isotope ratio in the gas phase,  $R_{ik, \text{cond}}$  is the isotope ratio in the condensed phase. Combining equations (3) and (4),  $\alpha_{ik}$  then becomes

$$\alpha_{ik} = \frac{P_{i, \text{sat}}/P_{k, \text{sat}}}{R_{ik, \text{cond}}} \frac{\gamma_i}{\gamma_k} \sqrt{\frac{m_k}{m_i}} \quad (5)$$

The equilibrium fractionation factor  $\alpha_{ik}^{\text{Eq}}$  and the kinetic fractionation factor  $\alpha_{ik}^{\text{Kin}}$  are defined in Eqs. (6) and (7), respectively (Richter, 2004; Dauphas and Rouxel, 2006; Richter et al., 2007).

$$\alpha_{ik}^{\text{Eq}} = \frac{P_{i, \text{sat}}/P_{k, \text{sat}}}{R_{ik, \text{cond}}} \quad (6)$$

$$\alpha_{ik}^{\text{Kin}} = \frac{\gamma_i}{\gamma_k} \sqrt{\frac{m_k}{m_i}} \quad (7)$$

The equilibrium isotope fractionations are negligible at the temperature of ~2005 °C in this study (i.e.,  $\alpha_{ik}^{\text{Eq}} = 1$ ). So we only consider the kinetic isotope fractionation here (i.e.,  $\alpha_{ik}^{\text{Kin}}$ ).

### 2.2. Classification of mass-dependent fractionation laws

Mass-dependent fractionation laws are commonly expressed using a power law that relates the mass-dependent fractionations for three isotopes, such that

$$\delta'_{ik} = \beta \times \delta'_{jk} \quad (8)$$

where *i*, *j*, and *k* are three isotopes of an element,  $\delta'$  is the isotope fractionation relative to a standard,  $[\delta'_{ik} = 1000 \times \ln(R_{ik, \text{sample}}/R_{ik, \text{std}})]$ , see further descriptions of  $\delta'$  for calcium and titanium isotopes in Section 3.3], and  $\beta$  depends on the fractionation law (Young et al., 2002; Young and Galy, 2004). MDF can occur both in nature

and in mass spectrometers. Due to instrumental MDF, isotope ratios measured in mass spectrometers always differ from the true ratios. A number of instrumental MDF laws have been proposed to correct instrumental MDF, including laws commonly labeled as “equilibrium”, “power”, “Rayleigh”, and “exponential” (e.g., Russell et al., 1978; Fahey et al., 1987; Hart and Zindler, 1989; Habfast, 1998; Maréchal et al., 1999; Albarède et al., 2004; Albarède and Beard, 2004). Maréchal et al. (1999) described a generalized power law (GPL) to represent the  $\beta$  value of all of these laws:

$$\beta = \frac{m_k^n - m_i^n}{m_k^n - m_j^n} \quad (9)$$

where  $m$  is the mass of the species containing isotope  $i, j$ , or  $k$ ;  $n = -1$  for the equilibrium law;  $n = 1$  for the power law;  $n$  approaches 0 for the exponential law; and  $n = -0.5$  for the Rayleigh law. Among them, the most widely accepted instrumental MDF law for TIMS data correction is the exponential law using the isotopic masses of individual atoms (rather than molecules). For example, Russell et al. (1978) and Hart and Zindler (1989) found that the exponential law best explained variations in calcium isotopic composition measured on standards using TIMS. Maréchal et al. (1999) also found that the exponential law adequately describes the mass fractionation in MC-ICPMS. However, MDF laws in natural processes are rarely studied. Most studies apply instrumental MDF laws, most commonly the exponential law, to correct naturally occurring MDFs (e.g., Niederer and Papanastassiou, 1984; Niederer et al., 1985; Leya et al., 2009; Trinquier et al., 2009; Huang et al., 2012). This practice needs to be carefully examined in high-precision isotope measurements of samples with significant natural MDF effects, as application of a fractionation law that does not describe natural fractionation can lead to spurious MIF effects. Furthermore, the nature of the MDF law bears clues on the nature of the processes responsible for this fractionation in natural samples.

### 3. EXPERIMENTAL AND ANALYTICAL TECHNIQUES

#### 3.1. Evaporation procedures

The evaporation experiments were carried out in 1994 at the University of Chicago using a vacuum furnace built by Dr. A. Hashimoto. Some details of the free evaporation procedure were described by Davis et al. (1995). Table 1 summarizes the experimental conditions. The two major oxide components of the starting material,  $\text{CaCO}_3$  (99.9995% purity) and  $\text{TiO}_2$  (99.999% purity), were fired in a platinum crucible at 1000 °C in air for three hours to convert the  $\text{CaCO}_3$  to  $\text{CaO}$  and remove any adsorbed volatiles. They were mixed and homogenized in the exact stoichiometric ratio, 1.0000:1.0000, of  $\text{CaTiO}_3$  perovskite. Three milligrams each of twenty-one trace elements (scandium, strontium, zirconium, niobium, barium, hafnium, tantalum, and all 14 stable rare earth elements) in their stable oxide forms were added to a small aliquot of the mixed  $\text{CaO} + \text{TiO}_2$  powder and

homogenized to make a concentrated oxide mixture. The final mixture contains  $\sim 100$  ppm each of twenty-one trace elements (0.2185 wt% total). The trace element fractionations were discussed by Davis et al. (1995). Ten aliquots of the final mixture,  $\sim 200$  mg each, were pressed into cylinders ( $\sim 6$  mm in diameter and  $\sim 5$  mm in height), holes were drilled through the axis of each cylinder, and all were fired at 1200 °C in air for an hour. They were trimmed with a razor blade to reduce their weight to  $157 \pm 1$  mg, and two samples were sintered in air, one for 17 h at 1425 °C (CT1425) and the other for 15 h at 1550 °C (CT1550). Elemental compositions of the starting material, as weighted and mixed and as measured by electron microprobe on CT1425 and CT1550, are given in Table 2. For each evaporation experiment, the sample was suspended in an iridium wire loop ( $\sim 4$  mm in diameter) at the center of a pair of hemicylindrical tungsten heaters ( $\sim 30$  mm in diameter and 130 mm in height), which in turn was enclosed within a fivefold tungsten (inner three layers) and molybdenum (outer two layers) radiation shield in the vacuum furnace. The shield had five large orifices (20–25 mm in diameter or U-shaped holes; two on sides for the heating electrodes, one in front for pyrometry, one on top and one at the bottom), which enabled efficient evacuation of vapor generated from the sample. A so-called, free (or Langmuir) evaporation condition was nearly achieved in this configuration, as had been demonstrated by the previous experimental work using the same furnace (Hashimoto et al., 1989; Hashimoto, 1990, 1991a; Richter et al., 2007). Overnight pre-evacuation reduced the pressure in the furnace to about  $5 \times 10^{-7}$  Torr, and the pressure remained in the lower  $10^{-6}$  Torr range during the entire heating stage. Temperature was measured by a Type G (tungsten – tungsten 26% rhenium) thermocouple and a one-color pyrometer; both were calibrated with the melting point of rhodium metal (1966 °C). A total of five evaporation experiments were carried out at a maximum temperature of  $\sim 2005$  °C in the vacuum furnace. The material remained molten throughout the evaporation experiments: the melting points of perovskite and  $\text{TiO}_2$  are  $\sim 1970$  and 1830 °C, respectively (Daněk and Nerád, 2002), and intermediate between the two endmember compositions is a eutectic at 1460 °C (Jacob and Gupta, 2009). It is thus unlikely that the evaporation experiments were limited by diffusion in the sample. At the beginning of each experiment, the iridium wire was threaded through the hole in the cylindrical sample, so that it was suspended above the loop. Upon melting, the sample filled the loop and was held in place by surface tension; its shape was nearly spherical at the start of melting and gradually flattened as evaporation and mass loss proceeded. The durations at the maximum temperatures of the five runs (CT-0.9 through CT-200) were  $\sim 0.9$ , 45, 100, 158, and 200 min, respectively. At the end of the prescribed duration of each evaporation run, the heater power was turned off to quench the evaporation residues. The evaporated fractions for CT-0.9, CT-45, CT-100, CT-158, and CT-200 relative to the mass of the starting material are 3.0%, 23.0%, 47.5%, 68.7%, and 83.4%, respectively.

Table 1  
Summary of the evaporation experiments.

Samples	Temp. (°C)	Time at peak temp. (min)	Initial mass (mg)	Final mass (mg)	% of initial mass remaining
<i>Starting materials</i>					
CT1425	1425	1000 (heated in air)			=100
CT1550	1550	900 (heated in air)			=100
<i>Evaporation residues</i>					
CT-0.9	2005	0.9	156.8	152.1	97.0
CT-45	2005	45	158.3	121.9	77.0
CT-100	2004	100	157.7	82.8	52.5
CT-158	2005	158	157.0	49.2	31.3
CT-200	2007	200	157.9	26.2	16.6

Table 2  
Element composition of starting materials and residues.

Samples	Starting materials				Evaporation residues			
	Mixture composition	CT 1425	CT1550	CT-0.9	CT-45	CT-100	CT-158	CT-200
%				3.0	23.0	47.5	68.7	83.4
Evap.								
<i>Electron microprobe</i>								
# anal.	As mixed	10	24	10	12	15	15	15
(wt.%)								
CaO	41.16	40.35 ± 0.13	41.42 ± 0.15	40.89 ± 0.09	32.6 ± 3.9	28.1 ± 3.9	24.6 ± 3.4	24.2 ± 3.6
TiO <sub>2</sub>	58.63	58.72 ± 0.11	58.96 ± 0.08	58.99 ± 0.09	67.4 ± 4.4	72.6 ± 4.3	76.9 ± 3.9	76.3 ± 4.2
MgO	0	0.000 ± 0.000	0.000 ± 0.000	0.000 ± 0.000	0.000 ± 0.000	0.000 ± 0.000	0.000 ± 0.000	0.000 ± 0.000
Al <sub>2</sub> O <sub>3</sub>	0	0.003 ± 0.001	0.004 ± 0.000	0.003 ± 0.001	0.003 ± 0.001	0.010 ± 0.002	0.012 ± 0.002	0.017 ± 0.004
SiO <sub>2</sub>	0	0.041 ± 0.027	0.014 ± 0.005	0.003 ± 0.001	0.001 ± 0.000	0.015 ± 0.002	0.014 ± 0.002	0.015 ± 0.003
<i>Scanning electron microscope (SEM)</i>								
# Anal.				10	10	10	10	10
CaO			41.12 ± 0.15*	40.6 ± 1.4	32.44 ± 0.89	28.48 ± 0.58	26.1 ± 1.2	24.5 ± 1.1
TiO <sub>2</sub>			59.47 ± 0.08*	59.5 ± 1.4	67.67 ± 0.90	71.56 ± 0.59	73.8 ± 1.1	75.2 ± 1.2

\* The SEM-EDS data of CT1550 are from calculations, not from direct measurement.

### 3.2. BSE imaging and major element composition analysis

Most of the sample characterization was done in 1994 and 1995. Backscattered electron (BSE) imaging and major element composition analysis of the two starting materials and five evaporation residues were carried out at the University of Chicago. BSE images and X-ray maps were taken using a Cameca SX-50 electron microprobe. The major element compositions were measured using the same electron microprobe, equipped with four wavelength-dispersive spectrometers for quantitative analysis. Analyses were conducted with a focused electron beam of 15 kV accelerating voltage and 25 nA beam current, resulting in an activation volume of  $\sim 1 \mu\text{m}^3$ . The data reduction was performed using the modified ZAF correction procedure PAP provided by Cameca (Pouchou and Pichoir, 1984). Ten to twenty-four spots were analyzed in each sample. The average of individual point analyses of each sample was calculated with the uncertainties reported as  $2\sigma$ . To check for homogeneity, the major element compositions of five evaporation residues were reanalyzed in 2012 using a JEOL JSM-5800LV scanning electron microscope (SEM) with an Oxford/Link ISIS-300 X-ray microanalysis system. Ten randomly chosen  $\sim 75 \times 100 \mu\text{m}$  rastered areas

(significantly larger than the grain size) were analyzed in each sample.

### 3.3. Calcium and titanium isotope analyses

Approximately 0.3–1 mg of each sample was crushed and weighed into a 6-mL Savillex PFA vial and dissolved in 1:3 of concentrated  $\text{HNO}_3$ : concentrated HF at  $\sim 180^\circ\text{C}$  in high-pressure Parr bombs following the method described by Zhang et al. (2011). After complete dissolution, the sample solution was dried and treated with concentrated  $\text{HNO}_3$ . This step was repeated three times to remove any trace HF. Then two separate aliquots were taken from each sample solution for calcium isotope measurements at Harvard University and for titanium isotope analysis at the Origins Lab of the University of Chicago.

Details of the calcium isotopic analytical procedure, which is applicable to variety of rocks and minerals, were described by Huang et al. (2010, 2012). Briefly, an aliquot of sample solution containing  $\sim 20 \mu\text{g}$  of calcium was mixed with an appropriate amount of a  $^{43}\text{Ca}$ – $^{48}\text{Ca}$  double spike solution, so that the  $^{40}\text{Ca}/^{48}\text{Ca}$  ratio of the sample to that of the spike was between 30 and 40. This range is optimal for determining mass-dependent calcium isotopic effects.



The spiked sample solution was then dried and dissolved in 40  $\mu\text{L}$  of 2.5 N HCl. This solution was then loaded onto a PFA microcolumn filled with 250  $\mu\text{L}$  cation exchange resin (BioRad AG50W-X12). Following the elution of matrix elements (*i.e.*, major element titanium, and trace elements magnesium, sodium, and potassium) with 1.55 mL of 2.5 N HCl, the calcium fraction was collected with additional 1.5 mL of 2.5 N HCl. All samples were passed through the column twice. The total procedural calcium blank is  $\sim 25$  ng (Huang et al., 2010). After chemical separation, calcium isotope ratios were measured with a GV Isoprobe-T Thermal Ionization Mass Spectrometer (TIMS). A two-step data acquisition sequence was used:  $^{40}\text{Ca}^+$ ,  $^{41}\text{K}^+$ ,  $^{42}\text{Ca}^+$ ,  $^{43}\text{Ca}^+$  and  $^{44}\text{Ca}^+$  in sequence 1 and  $^{44}\text{Ca}^+$  and  $^{48}\text{Ca}^+$  in sequence 2. Each measurement required  $\sim 5$   $\mu\text{g}$  Ca, and each sample was measured multiple times. Instrumental isotope fractionation, including fractionation both on cation columns and in the TIMS, was corrected using a  $^{43}\text{Ca}$ – $^{48}\text{Ca}$  double spike technique and an exponential law (Huang et al., 2010, 2011, 2012). Because of the limited sample sizes, no unspiked measurements were done, and the calcium isotopic composition of NIST SRM 915a was used as the unspiked measurement in the  $^{43}\text{Ca}$ – $^{48}\text{Ca}$  double spike calculation. Calcium isotope compositions are reported relative to NIST SRM915a in  $\delta'$  notation:

$$\delta^i\text{Ca} = 1000 \times \ln \frac{(i\text{Ca}/^{40}\text{Ca})_{\text{sample}}}{(i\text{Ca}/^{40}\text{Ca})_{\text{std}}} \quad (10)$$

where  $i$  represents 42 or 44.

Because the isotopic composition of our  $^{43}\text{Ca}$ – $^{48}\text{Ca}$  double spike is not absolute, the measured calcium isotopic compositions using  $^{43}\text{Ca}$ – $^{48}\text{Ca}$  double spike technique are not absolute, and are functions of the  $^{43}\text{Ca}/^{48}\text{Ca}$  ratio in our double spike solution. However, the calcium isotopic differences relative to NIST SRM 915a, *i.e.*, the  $\delta'$  values, are absolute and not dependent on the real isotopic composition of our double spike solution (see Huang et al., 2012 for a detailed discussion). The  $\delta'$ -value for some natural samples (*e.g.*, CAIs) includes both MDF and MIF, and there is no unique way to split the  $\delta'$ -value into MDF and MIF (*e.g.*, Niederer et al., 1985).

We are interested in examining whether any artificial MIF would be introduced after correction for MDF by assuming the exponential law. The MIF is reported in  $\epsilon$  notation:

$$\epsilon^i\text{Ca} = 10,000 \times \ln \left[ \frac{(i\text{Ca}/^{40}\text{Ca})_{\text{sample}}^*}{(i\text{Ca}/^{40}\text{Ca})_{\text{std}}^*} - 1 \right] \quad (11)$$

where  $i$  represents 40, 43, or 48 and the ratios marked with \* have been corrected for MDF by internal normalization to a fixed  $^{42}\text{Ca}/^{44}\text{Ca}$  ratio of 0.31221 using the exponential law (Niederer and Papanastassiou, 1984).

Titanium was separated via a two-stage procedure using TODGA and AG1-X8 resins (Zhang et al., 2011). The sample solution was dried and dissolved in 5 mL of 12 M  $\text{HNO}_3$  + 0.2 M  $\text{H}_3\text{BO}_3$ . It was then loaded onto a 2-mL TODGA cartridge, rinsed with 10 mL of 12 M  $\text{HNO}_3$  to remove matrix elements (*i.e.*, major element calcium, and trace elements magnesium, sodium, and potassium), and

titanium was collected with molybdenum and minor niobium, tantalum, and tungsten in 10 mL 12 M  $\text{HNO}_3$  + 1 wt%  $\text{H}_2\text{O}_2$ . The second separation stage was a modified version of a previously used procedure (Schönbacher et al., 2004), using a 0.8-mL column (AG1-X8). It removed major matrix with 10 mL 4 M HF independently from the first column and separated titanium from molybdenum, niobium, tantalum, and tungsten with 9 M HCl + 0.01 M HF. All samples were passed through the first column once and the second twice, yielding a full procedural blank of  $\sim 12$  ng. Titanium isotope analyses were measured with a Thermo Neptune Multicollector Inductively Coupled Plasma Mass Spectrometer (MC-ICPMS) using the sample-standard bracketing technique. Our bracketing standard, natural rutile from Kragerö, Norway, was also dissolved and processed through chemistry in the same way as the samples. Titanium isotope ratios were measured in two sequences on Faraday collectors (sequence 1 –  $^{44}\text{Ca}^+$ ,  $^{46}\text{Ti}^+$ ,  $^{47}\text{Ti}^+$ ,  $^{48}\text{Ti}^+$ ,  $^{49}\text{Ti}^+$  and  $^{50}\text{Ti}^+$ ; sequence 2 –  $^{49}\text{Ti}^+$ ,  $^{51}\text{V}^+$ , and  $^{52}\text{Cr}^+$ ). Titanium solutions in 2%  $\text{HNO}_3$  + 0.005% HF were introduced via two different desolvation inlet systems, an Elemental Scientific Inc. Stable Introduction System (SIS) dual cyclonic spray chamber and a CETAC Technologies Aridus II desolvating nebulizer system, with typical ion beam currents of  $\sim 1.5 \times 10^{-10}$  and  $\sim 7 \times 10^{-10}$  A, respectively on  $^{48}\text{Ti}$  for 1 ppm solution. All measurements were made at pseudo high-resolution mode, with  $m/(m_{0.95}-m_{0.05})$  of  $\sim 11,000$ . Titanium MDF is expressed in  $\delta'$  notation:

$$\delta^i\text{Ti} = 1000 \times \ln \left[ \frac{(i\text{Ti}/^{47}\text{Ti})_{\text{sample}}}{(i\text{Ti}/^{47}\text{Ti})_{\text{std}}} \right], \quad (12)$$

where  $i$  represents 46, 48, 49, or 50.

We are also interested in examining whether any artificial titanium MIF would be introduced after correction for MDF by assuming the exponential law. The titanium MIF is reported in  $\epsilon$  notation:

$$\epsilon^i\text{Ti} = 10,000 \times \ln \left[ \frac{(i\text{Ti}/^{47}\text{Ti})_{\text{sample}}^*}{(i\text{Ti}/^{47}\text{Ti})_{\text{std}}^*} - 1 \right], \quad (13)$$

where  $i$  represents 46, 48, or 50 and the ratios marked with \* have been corrected for MDF by internal normalization to a fixed  $^{49}\text{Ti}/^{47}\text{Ti}$  ratio of 0.749766 using the exponential law (Leya et al., 2008; Trinquier et al., 2009; Zhang et al., 2011). Analytical uncertainties for both calcium and titanium isotopic compositions are 95% confidence intervals.

Isotopic compositions are commonly reported in standard  $\delta$  notation, defined similarly to Eqs. (11) and (13), except that the multiplier is 1000, not 10,000. One reason for this usage is that on three isotope plots, *e.g.*,  $\delta^{50}\text{Ti}$  vs.  $\delta^{46}\text{Ti}$ , mixing lines are straight lines, but all of mass fractionation lines described by the generalized power law, Eq. (8), lie along curves. Since we are particularly concerned with mass fractionation laws in this work, we used  $\delta'$  notation, Eqs. (10) and (12), for which MDFs are plotted as straight lines on three-isotope plots.

## 4. RESULTS

### 4.1. BSE imaging

All experimental charges were in a completely molten state during evaporation and were crystallized upon quenching at the end of each experiment. The solid residues were examined using BSE imaging, shown in Fig. 1. The starting material (Fig. 1a) and the least evaporated residue CT-0.9 (Fig. 1b) are composed of single phase, perovskite, with some porosity. The melts evaporated incongruently, where calcium evaporated faster than titanium. The residue with higher degrees of evaporation than CT-0.9 quenched to mixtures of perovskite and titanium oxide (Fig. 1c–f). The proportion of perovskite decreased as the degree of

evaporation increased. In addition, the titanium oxide phase in the residues became more reduced as evaporation proceeded, as indicated by: (1) the progressively darker appearance of the residues; and (2) progressively higher total oxide percent of all phases beyond 100 wt% in the electron microprobe analyses, when all titanium was assumed to be present as  $\text{TiO}_2$ . There were also some variations in the BSE albedo of titanium oxide in late stage residues, indicating that they are mixtures of  $\text{TiO}_2$  and  $\text{Ti}_2\text{O}_3$ .

### 4.2. Elemental fractionation

Major element compositions in wt% measured by electron microprobe in 1995 and by SEM-EDS in 2012 on the solid residues are given in Table 2. The measurements

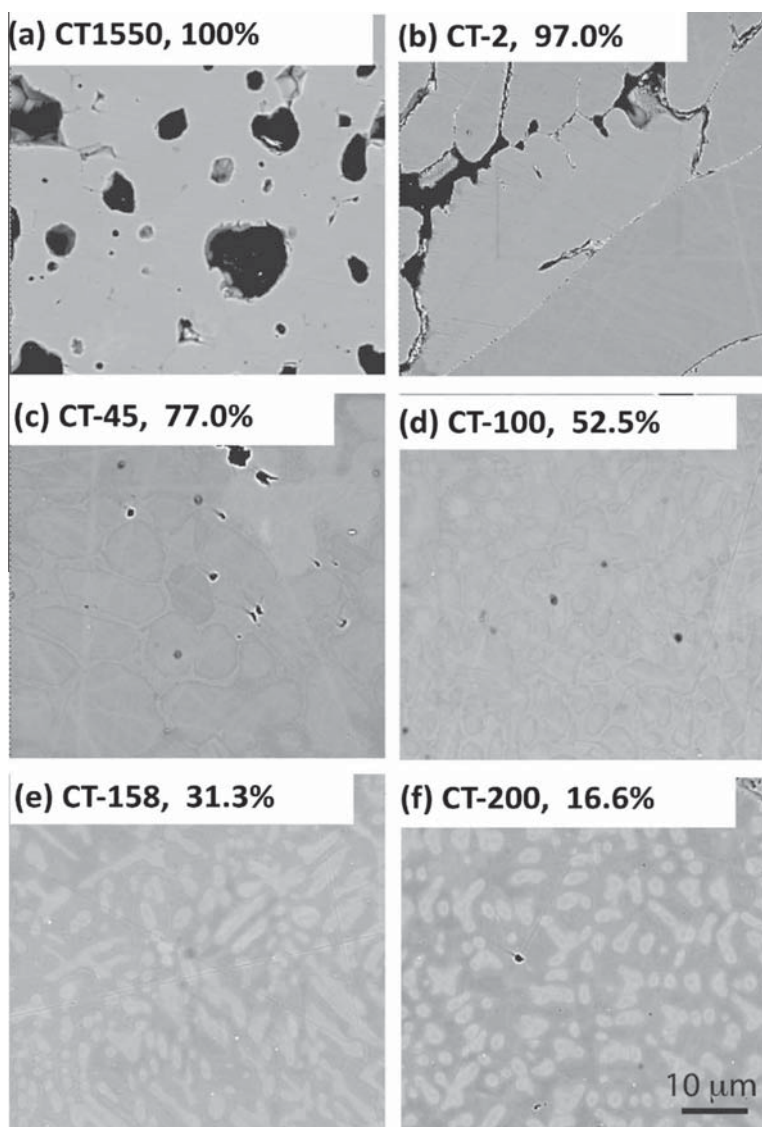


Fig. 1. Backscattered electron images of the starting material (a) and five residues (b–f) from evaporation of  $\text{CaTiO}_3$ . The starting material is composed of a single phase (in gray) with some porosity (in black). Evaporation residues produced by quenching and crystallization of liquids are mixtures of perovskite (in light gray) and titanium oxide (in dark gray). The proportion of perovskite decreases as the degree of evaporation increases from CT-0.9 (b) to CT-200 (f). The scale bar is 10  $\mu\text{m}$ .

with the two techniques are in good agreement within uncertainties, but the SEM-EDS results are of higher precision than those from electron microprobe for mixed phase residues (from CT-45 to CT-200). That is because rastering the beam during SEM analysis reduced the scatter by averaging the various individual phases, whereas the spot analysis using the electron microprobe measured single phases and averaged them. In contrast, CT-0.9 is composed of a single phase and the data from electron microprobe are more precise than those from the SEM. To be consistent, hereafter we used the SEM-EDS data for all five

evaporation residues. For the starting materials, it would be preferable to use SEM-EDS data as well for consistency in calculating the loss fraction of Ca (Table 3) and Ti (Table 4). However, the starting materials were all digested and their splits are no longer available, so we inferred the CaO and TiO<sub>2</sub> abundances of CT1550 expected in SEM-EDS measurement to be 41.12 and 59.47 wt%, respectively, using the data for CT-0.9 from two techniques and the data for the starting materials from electron microprobe only, and assuming that the abundance bias between the electron microprobe measurement and the SEM-EDS measurement

Table 3  
Calcium isotopic compositions of evaporation samples.

Samples	$-\ln(f^{40}\text{Ca})^{\S}$	$\delta^{44}\text{Ca}_{\text{SRM915a}}$	$\delta^{42}\text{Ca}_{\text{SRM915a}}$	$\delta^{44}\text{Ca}^*$	$\delta^{42}\text{Ca}^*$	$\varepsilon^{40}\text{Ca}$	n
<i>Starting materials</i>							
CT1425		$0.93 \pm 0.06$	$0.50 \pm 0.08$				4
CT1550		$0.91 \pm 0.08$	$0.47 \pm 0.04$				3
Grand average		$0.92 \pm 0.05$	$0.49 \pm 0.05$	$0.00 \pm 0.00$	$0.00 \pm 0.00$	$0.00 \pm 0.00$	
<i>Evaporation residues</i>							
CT-0.9	$0.032 \pm 0.004$	$2.30 \pm 0.07$	$1.21 \pm 0.11$	$1.37 \pm 0.09$	$0.72 \pm 0.12$	$-0.49 \pm 0.09$	4
CT-45	$0.487 \pm 0.027$	$21.22 \pm 0.04$	$11.03 \pm 0.03$	$20.30 \pm 0.06$	$10.54 \pm 0.06$	$-3.08 \pm 0.06$	4
CT-100	$1.000 \pm 0.021$	$41.01 \pm 0.05$	$21.19 \pm 0.06$	$40.08 \pm 0.07$	$20.70 \pm 0.08$	$-4.23 \pm 0.07$	5
CT-158	$1.603 \pm 0.046$	$72.49 \pm 0.08$	$37.57 \pm 0.04$	$71.57 \pm 0.10$	$37.08 \pm 0.06$	$-9.52 \pm 0.09$	5
CT-200	$2.300 \pm 0.043$	$100.10 \pm 0.06$	$51.84 \pm 0.10$	$99.18 \pm 0.08$	$51.35 \pm 0.11$	$-12.77 \pm 0.06$	5

\* Calcium isotopic compositions were calculated based on the equation:  $\delta'Ca_{\text{sample-starting material}} = \delta'Ca_{\text{sample-SRM 915a}} - \delta'Ca_{\text{starting material-SRM 915a}}$ .

<sup>§</sup>  $-\ln(f^{40}\text{Ca})$  was calculated using equation:  $-\ln(f^{40}\text{Ca}) = \frac{F_f \times C_{\text{CaO},f} \times A_{40,\text{Ca},f}}{C_{\text{CaO},i} \times A_{40,\text{Ca},i}}$ , where  $F_f$  is the fraction of initial mass remaining (Table 1),  $C_{\text{CaO},f}$  and  $C_{\text{CaO},i}$  are the CaO concentrations for evaporation residue and the starting material, respectively (Table 2),  $A_{40,\text{Ca},f}$  and  $A_{40,\text{Ca},i}$  are  $^{40}\text{Ca}$  abundances for evaporation residue and the starting material, respectively.

Table 4  
Titanium isotopic compositions of evaporation samples.

		Spray Chamber					
Samples	$-\ln(f^{47}\text{Ti})$	$\delta^{46}\text{Ti}$	$\delta^{48}\text{Ti}$	$\delta^{49}\text{Ti}$	$\delta^{50}\text{Ti}$	$\varepsilon^{50}\text{Ti}$	$n$
<i>Starting materials</i>							
CT1425		$-0.01 \pm 0.04$	$0.02 \pm 0.05$	$0.03 \pm 0.07$	$0.04 \pm 0.11$	$-0.01 \pm 0.14$	11
CT1550		$0.00 \pm 0.08$	$0.02 \pm 0.12$	$0.04 \pm 0.19$	$0.05 \pm 0.30$	$-0.02 \pm 0.17$	9
<i>Evaporation residues</i>							
CT-0.9	$0.029 \pm 0.005$	$0.05 \pm 0.24$	$0.07 \pm 0.15$	$0.09 \pm 0.13$	$0.10 \pm 0.21$	$-0.28 \pm 0.42$	11
CT-45	$0.132 \pm 0.014$	$-0.85 \pm 0.09$	$0.84 \pm 0.11$	$1.66 \pm 0.20$	$2.47 \pm 0.31$	$-0.02 \pm 0.25$	9
CT-100	$0.461 \pm 0.009$	$-2.94 \pm 0.06$	$2.88 \pm 0.09$	$5.72 \pm 0.13$	$8.49 \pm 0.21$	$0.15 \pm 0.21$	11
CT-158	$0.950 \pm 0.015$	$-5.93 \pm 0.08$	$5.86 \pm 0.13$	$11.57 \pm 0.20$	$17.18 \pm 0.32$	$0.04 \pm 0.26$	9
CT-200	$1.569 \pm 0.016$	$-9.61 \pm 0.49$	$9.34 \pm 0.28$	$18.56 \pm 0.09$	$27.59 \pm 0.13$	$0.45 \pm 0.70$	11
		Aridus II					
		$\delta^{46}\text{Ti}$	$\delta^{48}\text{Ti}$	$\delta^{49}\text{Ti}$	$\delta^{50}\text{Ti}$	$\varepsilon^{50}\text{Ti}$	$n$
<i>Starting materials</i>							
CT1425		$-0.02 \pm 0.03$	$-0.02 \pm 0.04$	$0.01 \pm 0.03$	$0.00 \pm 0.04$	$-0.07 \pm 0.11$	11
CT1550		$0.02 \pm 0.02$	$0.00 \pm 0.01$	$-0.02 \pm 0.03$	$-0.03 \pm 0.04$	$0.04 \pm 0.06$	9
<i>Evaporation residues</i>							
CT-0.9		$-0.09 \pm 0.04$	$0.02 \pm 0.05$	$0.10 \pm 0.02$	$0.14 \pm 0.04$	$-0.08 \pm 0.14$	11
CT-45		$-0.89 \pm 0.02$	$0.88 \pm 0.01$	$1.73 \pm 0.02$	$2.57 \pm 0.03$	$0.04 \pm 0.07$	9
CT-100		$-2.95 \pm 0.03$	$2.87 \pm 0.05$	$5.71 \pm 0.05$	$8.48 \pm 0.07$	$0.02 \pm 0.08$	11
CT-158		$-6.00 \pm 0.02$	$5.85 \pm 0.02$	$11.62 \pm 0.02$	$17.26 \pm 0.04$	$0.11 \pm 0.06$	9
CT-200		$-9.60 \pm 0.09$	$9.36 \pm 0.07$	$18.59 \pm 0.03$	$27.62 \pm 0.03$	$0.26 \pm 0.23$	11

<sup>§</sup>  $-\ln(f^{47}\text{Ti})$  was calculated using equation:  $-\ln(f^{47}\text{Ti}) = \frac{F_f \times C_{\text{TiO}_2,f} \times A_{47,\text{Ti},f}}{C_{\text{TiO}_2,i} \times A_{47,\text{Ti},i}}$ , where  $F_f$  is the fraction of initial mass remaining (Table 1),  $C_{\text{TiO}_2,f}$  and  $C_{\text{TiO}_2,i}$  are the TiO<sub>2</sub> concentrations for evaporation residue and the starting material, respectively (Table 2),  $A_{47,\text{Ti},f}$  and  $A_{47,\text{Ti},i}$  are  $^{47}\text{Ti}$  abundances for evaporation residue and the starting material, respectively.

is constant for single-phase samples. On the other hand, we took the uncertainties from electron microprobe measurements as the uncertainties of the expected SEM-EDS values for CT1550, because they came from 24 spot measurements and should reasonably reflect the variation of abundances within a single-phase sample. The relationship between the bulk chemical composition (CaO and TiO<sub>2</sub>) and the percent weight loss of the residue is plotted in Fig. 2a. This figure shows that the CaO concentration decreases from 41.12 to 24.55 wt% with increasing weight loss, while TiO<sub>2</sub> concentration increases from 59.47 to 75.24 wt%. This demonstrates again that liquids of initial CaTiO<sub>3</sub> composition preferentially evaporated calcium over titanium. The percentage weight loss of TiO<sub>2</sub> and CaO as a function of time at 2005 °C are shown in Fig. 2b.

#### 4.3. Calcium and titanium mass-dependent fractionations (MDFs)

Calcium MDFs are given in Table 3. Relative to NIST SRM915a, the starting material has  $\delta^{44}\text{Ca}_{\text{SRM915a}}$  and  $\delta^{42}\text{Ca}_{\text{SRM915a}}$  values of  $+0.92 \pm 0.05\text{‰}$  and  $+0.49 \pm 0.05\text{‰}$ , respectively. After standardizing to these values,  $\delta^i\text{Ca}_{\text{start}}^{\text{sample}} = \delta^i\text{Ca}_{\text{SRM915a}}^{\text{sample}} - \delta^i\text{Ca}_{\text{SRM915a}}^{\text{start}}$ , we find that the evaporation residues are all enriched in heavy calcium isotopes compared to the starting material.

Table 4 shows titanium MDFs of evaporation samples measured using two different inlet systems, the SIS spray chamber and the Aridus II desolvating nebulizer. The results are in good agreement within the uncertainties, but the data from the Aridus II have 2–10 times better precision than that from the spray chamber, so only the data from the Aridus II will be discussed hereafter. Relative to our bracketing standard (Krageroë rutile), the two starting materials CT1425 and CT1550 show no MDFs for titanium, with  $\delta^{50}\text{Ti}$  values of  $0.00 \pm 0.04$  and  $-0.03 \pm 0.04$ , respectively. Thus, it was not necessary to standardize the titanium MDF to the evaporation starting material. The five evaporation residues are all fractionated and their titanium isotopic compositions are enriched in the heavy isotopes (Table 4).

## 5. DISCUSSION

### 5.1. Evaporating species

The nature of the evaporating species influences the mass-dependent fractionation during evaporation process. The free evaporation in our experiments follows a Rayleigh distillation process. Rayleigh distillation behavior is described as

$$\frac{R_{ik}}{R_{ik,0}} = f_k^{\alpha_{ik}-1}, \quad (14)$$

where  $R_{ik,0}$  is the isotopic ratio in the condensed phase prior to evaporation and  $R_{ik}$  is the isotopic ratio in the evaporation residue when a fraction  $f_k$  of isotope  $k$  remains. By taking the natural logarithm of both sides, Eq. (14) can be rewritten as

$$\delta'_{ik} = 1000 \times \ln \left( \frac{R_{ik}}{R_{ik,0}} \right) = 1000 \times (\alpha_{ik} - 1) \times \ln f_k \quad (15)$$

Linear relationships between measured MDF ( $\delta'_{ik}$ ) and the degree of evaporation ( $\ln f_k$ ) are found for both calcium (Fig. 3a) and titanium (Fig. 3b), indicating that the evaporation is in accord with Rayleigh distillation. The experimental fractionation factors  $\alpha_{44\text{Ca}/40\text{Ca}}$  and  $\alpha_{49\text{Ti}/47\text{Ti}}$  (hereafter  $\alpha_{\text{Ca}}$  and  $\alpha_{\text{Ti}}$ , respectively) can be derived from the slopes [slope =  $1000 \times (\alpha_{ik} - 1)$ ] of the best linear fit (red lines in Fig. 3). The derived experimental fractionation factors  $\alpha_{\text{Ca}}$  and  $\alpha_{\text{Ti}}$  are  $0.9562 \pm 0.0040$  (Fig. 3a) and  $0.9881 \pm 0.0007$  (Fig. 3b), respectively. Theoretical isotopic fractionation factors are calculated using the inverse square root of the mass of the evaporating species assuming that the evaporation coefficients are independent of the mass of the isotopes ( $\alpha_{ik} = \sqrt{m_k/m_i}$  with  $\gamma_i = \gamma_k$  in Eq. (7)). One should keep in mind that the assumption that  $\gamma$  does not depend on the isotope mass may not be correct, as indicated by previous experiments of magnesium evaporation from CAI-like liquid for which the values of  $\alpha$  are always lower than expected (Richter et al., 2007 and references therein). The theoretical values of  $\alpha$  were calculated for the possible evaporating species assuming non

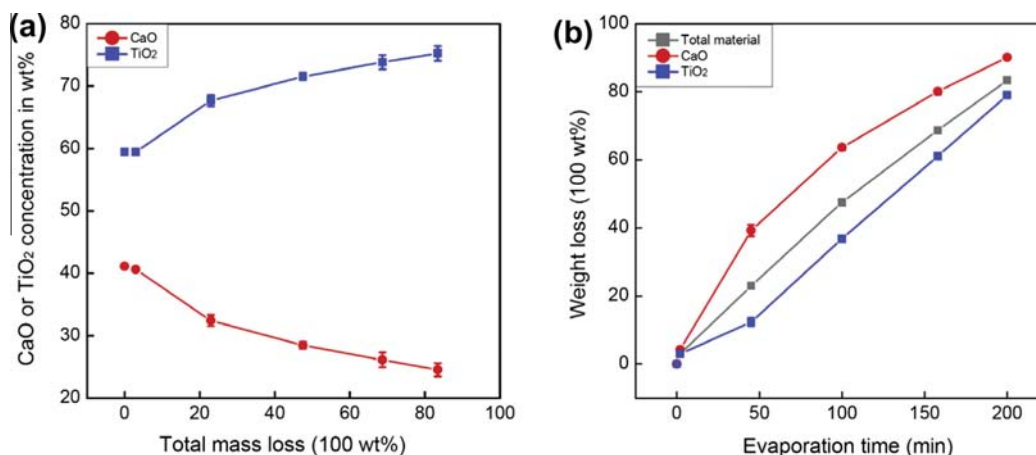


Fig. 2. Major element compositions of the starting material and five residues from evaporation of CaTiO<sub>3</sub>. (a) Plot of CaO and TiO<sub>2</sub> in wt.% vs. percent of total mass loss. (b) Weight loss amounts of CaO, TiO<sub>2</sub>, and total material as a function of the evaporation time.



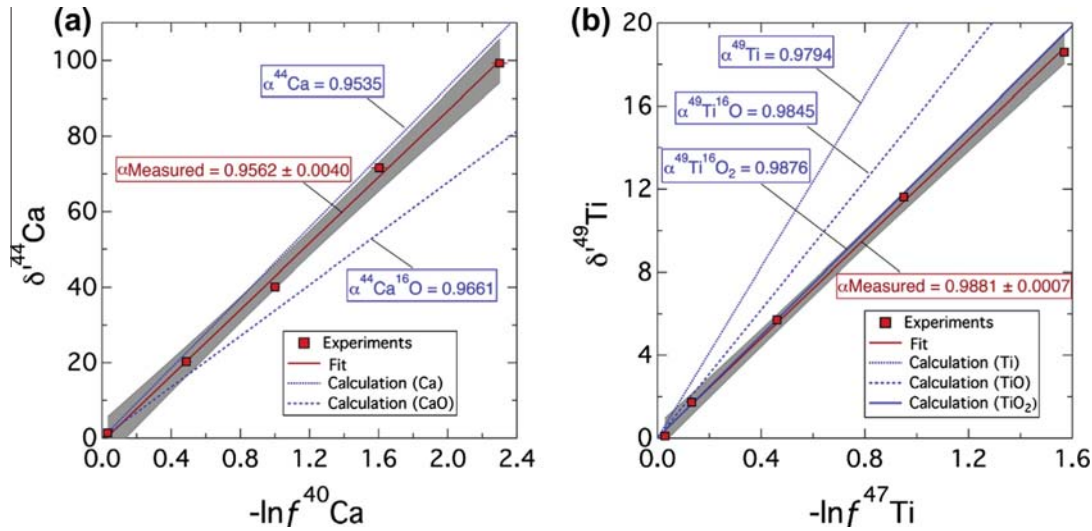
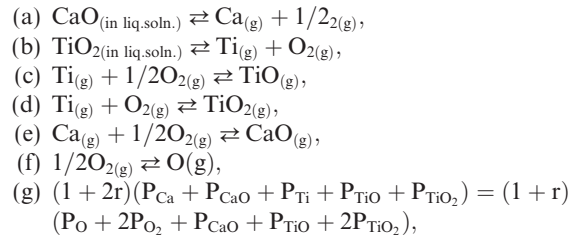


Fig. 3. (a)  $\delta^{44}\text{Ca}$  vs.  $-\ln f^{40}\text{Ca}$  and (b)  $\delta^{49}\text{Ti}$  vs.  $-\ln f^{47}\text{Ti}$  in five evaporation residues (red squares).  $f$  is the fraction of  $^{40}\text{Ca}$  or  $^{47}\text{Ti}$  abundance remaining in the residue. Linear regressions are shown (red lines), with 95 % confidence envelopes (gray areas) using unweighted orthogonal distance regression in the program Igor Pro. The blue lines represent theoretical fractionations, obtained with the fractionation factors calculated from the inverse square roots of the masses of the evaporating species (Ca atoms, CaO molecules, Ti atoms, TiO, or  $\text{TiO}_2$  molecules). (For interpretation of the references to colour in this figure legend, the reader is referred to the web version of this article.)

mass-dependence of  $\gamma$ : Ca atoms (0.9535), CaO molecules (0.9661), Ti atoms (0.9794), TiO (0.9845) and  $\text{TiO}_2$  molecules (0.9876), and the results are also plotted in Fig. 3 (blue lines). Fig. 3 shows that measured fractionation factors are consistent with Ca and  $\text{TiO}_2$  as the dominant evaporating species during the evaporation of liquid  $\text{CaTiO}_3$ , provided that the ratios of evaporation coefficients of isotopes ( $\gamma^{44}\text{Ca}/^{40}\text{Ca}$  and  $\gamma^{50}\text{Ti}/^{46}\text{Ti}$ ) are approximately equal to one (see Eq. (7)).

Wang et al. (1999) used equilibrium thermodynamic calculations to predict that the major evaporating species for magnesium and silicon from molten or solid  $\text{Mg}_2\text{SiO}_4$  are Mg atoms and SiO molecules, respectively, just as Nichols et al. (1995, 1998) had measured by mass spectrometry during Knudsen cell and Langmuir evaporation. The same general approach has been used previously for evaporation of magnesium and silicon from CAI melts (e.g., Grossman et al., 2000; Richter et al., 2002), where equilibrium thermodynamic calculations showed that the gas-phase species were Mg and SiO. The thermodynamic approach is much more robust than earlier energetic and entropic considerations that led to the erroneous conclusion that  $\text{SiO}_2$  was a significant gas-phase species in free evaporation of forsterite (Hashimoto, 1990). We did thermodynamic calculations that indicate the dominant evaporating species in equilibrium with a melt of  $\text{CaTiO}_3$  at 2005 °C were Ca and  $\text{TiO}_2$ . We calculated equilibrium partial pressures of the gas-phase species above molten  $\text{CaTiO}_3$  at 2005 °C using thermodynamic data (Robie et al., 1979; Chase, 1998; Shornikov, 2011). Our experimental data shows that  $\text{CaTiO}_3$  evaporates incongruently, so it is necessary to use the activities of the CaO and  $\text{TiO}_2$  components in molten  $\text{CaTiO}_3$  (Shornikov, 2011). The calculation does not require congruent evaporation, but does assume that all

condensed-phase titanium is tetravalent. We have six reactions (Eqs. a–f) and one valence-stoichiometry equation (Eq. g):



where  $r = (P_{\text{Ti}} + P_{\text{TiO}} + P_{\text{TiO}_2})/(P_{\text{Ca}} + P_{\text{CaO}})$  (See details in Appendix) and  $P$  is the partial pressure. With this set of equations and the set ‘A’ of  $\log_{10}(\text{activities})$  of CaO and  $\text{TiO}_2$ ,  $-1.6$  and  $-0.65$  (Shornikov and Archakov, 2003), the calculation yields the following partial pressures:  $P_{\text{Ca}} = 1.9 \times 10^{-6}$  bar;  $P_{\text{CaO}} = 9.4 \times 10^{-9}$  bar;  $P_{\text{Ti}} = 1.2 \times 10^{-10}$  bar;  $P_{\text{TiO}} = 3.9 \times 10^{-7}$  bar;  $P_{\text{TiO}_2} = 3.2 \times 10^{-6}$  bar;  $P_{\text{O}} = 1.9 \times 10^{-6}$  bar; and  $P_{\text{O}_2} = 2.0 \times 10^{-7}$  bar.  $\text{Ca}_{(\text{g})}$  and  $\text{TiO}_{2(\text{g})}$  are the most abundant gas species for calcium and titanium, respectively, and the latter partial pressure is higher than the former. With the set ‘B’ of  $\log_{10}(\text{activities})$  of CaO and  $\text{TiO}_2$ ,  $-1.15$  and  $-0.95$  (Shornikov, 2011), respectively, the results are as follows:  $P_{\text{Ca}} = 3.6 \times 10^{-6}$  bar;  $P_{\text{CaO}} = 2.7 \times 10^{-8}$  bar;  $P_{\text{Ti}} = 2.7 \times 10^{-11}$  bar;  $P_{\text{TiO}} = 1.3 \times 10^{-7}$  bar;  $P_{\text{TiO}_2} = 1.6 \times 10^{-6}$  bar;  $P_{\text{O}} = 2.9 \times 10^{-6}$  bar;  $P_{\text{O}_2} = 4.4 \times 10^{-7}$  bar. Again,  $\text{Ca}_{(\text{g})}$  and  $\text{TiO}_{2(\text{g})}$  are the most abundant gas species for each element, but the partial pressure of  $\text{Ca}_{(\text{g})}$  is twice as large as that of  $\text{TiO}_{2(\text{g})}$ . We have, for the moment, no preference between the two sets of oxide activities, but this will be further discussed in Section 5.2. However, it is evident that  $\text{Ca}_{(\text{g})}$  and  $\text{TiO}_{2(\text{g})}$

are by far the most abundant gas species for each element in equilibrium with liquid  $\text{CaTiO}_3$  at 2005 °C. It would be desirable to use mass spectrometry or other techniques to ascertain the nature of the evaporating species in our experiments.

## 5.2. Evaporation coefficients for calcium and titanium elements

The evaporation coefficients of metals are usually close to unity (Hirth and Pound, 1963; Tachibana et al., 2011), but this is not always true for oxides and silicates, mostly due to the decomposition and recombination processes of various molecules and atoms occurring on the surface of condensed phase (Somorjai and Lester, 1967; Sata et al., 1978; Hashimoto, 1990; Nagahara and Ozawa, 1996; Tsuchiyama et al., 1998; Kuroda and Hashimoto, 2002; Richter et al., 2007; Takigawa et al., 2009). We estimated evaporation coefficients for elements calcium and titanium from the liquid  $\text{CaTiO}_3$  based on our evaporation residue CT-0.9 using Eq. (2) in Section 2, because CT-0.9 was heated rapidly and spent only 54 s at the run temperature of 2005 °C. Thus, its chemical composition did not change significantly and the shape of the charge was nearly spherical so that its surface area can be accurately determined. The moles of evaporated calcium and titanium ( $\Delta N_{\text{exp}}$ ; mol) from the liquid  $\text{CaTiO}_3$  can be calculated using equation:

$$\Delta N_{\text{exp}} = (M_i \times C_i - M_f \times C_f) / m \quad (16)$$

where  $M_i$  and  $M_f$  are the initial and final mass of evaporation residue CT-0.9, respectively, given in Table 1,  $C_i$  and  $C_f$  are the initial and final weight concentrations of Ca or  $\text{TiO}_2$ , respectively, given in Table 2,  $m$  is the molar mass of Ca or  $\text{TiO}_2$ . We used CT-0.9 for the final mass and final weight abundances (electron microprobe data) and used CT1550 for the initial mass and initial weight abundances (electron microprobe data). The calculated number of moles evaporated for Ca and  $\text{TiO}_2$  are  $4.9 \times 10^{-5}$  and  $3.4 \times 10^{-5}$  mol, respectively. The evaporation coefficient ( $\gamma_i$ ) is calculated by taking the ratio of the measured number of moles evaporated ( $\Delta N_{\text{exp}}$ ) to that calculated by assuming that vapor species would impinge on the condensed surface at equilibrium (i.e., saturation); the latter corresponds to the theoretical number of moles evaporated  $\Delta N_{\text{theory}}$

$$\Delta N_{\text{theory}} = \frac{\gamma_i P_{i,\text{sat}}}{\sqrt{2\pi m_i RT}} \times A \times t, \quad (17)$$

where  $A$  is sample surface area and  $t$  is the evaporation duration. CT-0.9 had a complex thermal history as opposed to the rest of evaporation residues: it had a dwell stage at 1700 °C, four ramping (up and down) steps, and a second dwell stage at 2005 °C. The combined duration, 0.9 min, of the dwell at 2005 °C was short compared to the time used for the ramping steps. Thus evaporation during ramping is no less important than the evaporation at the dwell stages. However, since we only need an order-of-magnitude estimate of the evaporation coefficient, we simply used fixed values of the activities at 2005 °C in the calculations, instead of the temperature-dependent activities. The

theoretical, temperature–time integration of the evaporation rate for the entire heating procedure of CT-0.9 gives (1)  $\Delta N_{\text{theory,Ca}} = 5.4 \times 10^{-5}$  mol;  $\Delta N_{\text{theory,TiO}_2} = 4.2 \times 10^{-5}$  mol for activity set A, and (2)  $\Delta N_{\text{theory,Ca}} = 1.0 \times 10^{-4}$  mol;  $\Delta N_{\text{theory,TiO}_2} = 2.3 \times 10^{-5}$  mol for set B, where  $\Delta N_{\text{theory}}$  indicates a theoretical calculation. The sample surface area for CT-0.9 used in the above calculation,  $0.578 \text{ cm}^2$ , was estimated from the observed spherical shape, the average mass of the charge before and after the experiment, and the density of liquid  $\text{CaTiO}_3$  at 2005 °C ( $3.74 \text{ g cm}^{-3}$ ). It is notable that the total evaporated calcium-bearing species (in moles) exceeds that of titanium-bearing species. We can estimate evaporation coefficients of calcium and titanium from the  $\text{CaTiO}_3$  liquid and the results are: (1)  $\gamma_{\text{Ca}} = 0.90$  and  $\gamma_{\text{Ti}} = 0.80$  (−1.6 and −0.65 for  $\log_{10}(\text{activity})$  of CaO and  $\text{TiO}_2$ , respectively) activity set A; and (2)  $\gamma_{\text{Ca}} = 0.485$  and  $\gamma_{\text{Ti}} = 1.5$  (−1.15 and −0.95, respectively) for activity set B. The evaporation coefficients are smaller than unity, except for titanium in the set B. The activity data for the set A are based on a Knudsen mass spectrometric measurement (Shornikov and Archakov, 2003), and are preferred to the set B which is a model calculation (Shornikov, 2011). A previous study of evaporation coefficients for pure solid CaO and pure solid and liquid  $\text{TiO}_2$  (Hashimoto et al., 1989) revealed that  $\gamma_{\text{Ca}}$  is 0.9, and  $\gamma_{\text{Ti}}$  is 0.39 for solid  $\text{TiO}_2$  and 0.41 for liquid  $\text{TiO}_2$ . The evaporation coefficient of CaO was also studied for various compounds (Hashimoto et al., 1989; Hashimoto, 1991b): liquid  $\text{CaAl}_2\text{O}_4$  ( $\gamma_{\text{Ca}} = 0.8$ –1.2); solid and liquid gehlenite composition,  $\text{Ca}_2\text{Al}_2\text{SiO}_7$  ( $\gamma_{\text{Ca}} \sim 1$ ); and liquid åkermanite composition,  $\text{Ca}_2\text{MgSi}_2\text{O}_7$  ( $\gamma_{\text{Ca}} \sim 1$ ). Although the compounds required activity values from a proper liquid solution model (e.g., Hashimoto, 1991c) in determining equilibrium partial vapor pressures, they unequivocally exhibited  $\gamma_{\text{Ca}} \sim 1$ . Compared with the  $\gamma_{\text{Si}} = 0.05$ –0.16 and  $\gamma_{\text{Mg}} = 0.04$ –0.18 in the temperature range 1500–1900 °C in previous studies (Richter et al., 2002, 2007), the result of the set A,  $\gamma_{\text{Ca}} = 0.90$ , is rather close to unity, and  $\gamma_{\text{Ti}} = 0.80$  is also close to unity.

The evaporation coefficients determined above can be applied to many other studies. For example, evaporation coefficients are required in the calculation of the evolutionary paths of the chemical composition of CAI liquids during evaporation (Grossman et al., 2000). Also, evaporation coefficients are parameters that affect the timescale of equilibration between Earth's mantle and the protolunar disk. Zhang et al. (2012a) had assumed  $\gamma_{\text{Ca}} = 1$  and  $\gamma_{\text{Ti}} = 1$ , which are approximately correct for the composition measured here. However, it remains to be determined whether these near-unity coefficients are also applicable to silicate melt compositions.

## 5.3. Mass-dependent fractionation (MDF) laws for calcium and titanium isotopes

Fractionation of calcium isotopes in natural samples, including CAIs, has been inferred to follow an exponential law (e.g., Huang et al., 2010, 2011, 2012; Farkaš et al., 2011). However, the samples upon which this inference was based exhibit relatively small  $F_{\text{Ca}}$  [ $<2\%$  per amu,

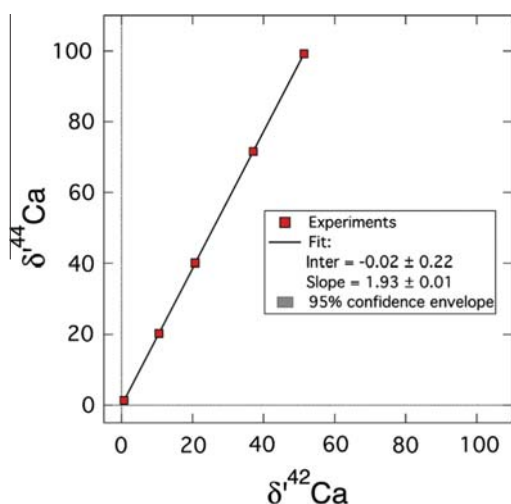


Fig. 4.  $\delta^{44}\text{Ca}$  vs.  $\delta^{42}\text{Ca}$  in evaporation residues (red squares). A linear correlation was found with a best-fit slope of  $1.93 \pm 0.01$  using weighted orthogonal distance regression in the program Igor Pro. The comparison with theoretical fractionation lines following exponential law, the Rayleigh law, equilibrium law, and power law is shown in Fig. 6a. Here 95% confidence envelopes are too narrow to be visible.

$F_{\text{Ca}} = \delta^{42}\text{Ca}/(m^{42}\text{Ca}-m^{40}\text{Ca})$ , and such a limited fractionation range may not allow different fractionation laws to be distinguished. In contrast, the titanium isotope MDF law in natural samples has never been studied. As noted earlier, it is difficult to find natural examples with sufficient isotopic fractionations of calcium and titanium to test their MDF laws. Although some natural CAIs have large calcium and titanium isotopic fractionations, the issue is complicated by the presence of calcium and titanium nucleosynthetic anomalies with  $\epsilon^{48}\text{Ca}$  and  $\epsilon^{50}\text{Ti}$  up to  $1046 \pm 41$  and  $2729 \pm 50$ , respectively (e.g., Ireland, 1990; Ireland et al., 1992). Here, laboratory free-evaporation residues from our experiments show significant MDFs of calcium and titanium, allowing us to determine the evaporation MDF laws.

Since Ca and  $\text{TiO}_2$  are the dominant evaporating species in these experiments (Section 5.1), we investigate the evaporation MDF laws for Ca and  $\text{TiO}_2$ . A linear correlation was found between  $\delta^{44}\text{Ca}$  vs.  $\delta^{42}\text{Ca}$  for five evaporation residues (Fig. 4), with a best-fit slope of  $1.93 \pm 0.01$  ( $2\sigma$ ). Linear correlations were also found for  $\delta^{49}\text{Ti}$  vs.  $\delta^{48}\text{Ti}$ ,  $\delta^{50}\text{Ti}$  vs.  $\delta^{46}\text{Ti}$ ,  $\delta^{49}\text{Ti}$  vs.  $\delta^{46}\text{Ti}$ , and  $\delta^{48}\text{Ti}$  vs.  $\delta^{46}\text{Ti}$  (Fig. 5a–d, respectively) for the five evaporation residues. The best-fit slopes are of  $1.99 \pm 0.01$ ,  $-2.88 \pm 0.02$ ,  $-1.94 \pm 0.01$ , and  $-0.97 \pm 0.02$ , respectively (all  $2\sigma$ ). These

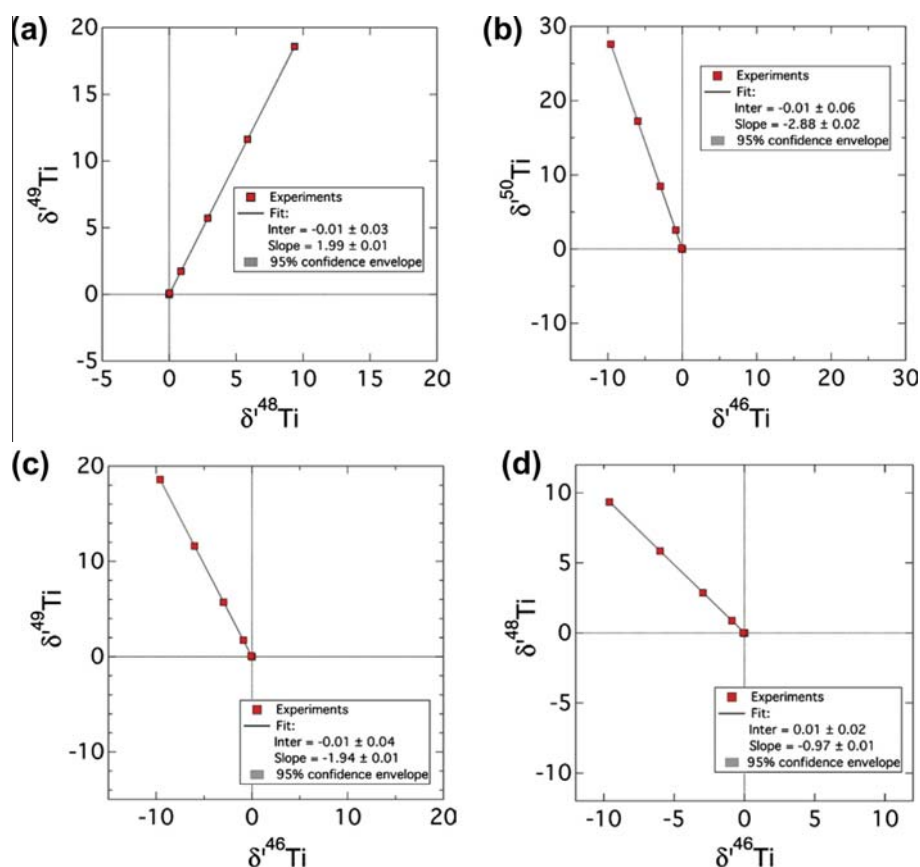


Fig. 5. (a)  $\delta^{49}\text{Ti}$  vs.  $\delta^{48}\text{Ti}$ , (b)  $\delta^{50}\text{Ti}$  vs.  $\delta^{46}\text{Ti}$ , (c)  $\delta^{49}\text{Ti}$  vs.  $\delta^{46}\text{Ti}$ , and (d)  $\delta^{48}\text{Ti}$  vs.  $\delta^{46}\text{Ti}$  in evaporation residues (red squares). Linear correlations were found with best-fit slopes of  $1.99 \pm 0.01$ ,  $-2.88 \pm 0.02$ ,  $-1.94 \pm 0.01$  and  $-0.97 \pm 0.01$ , respectively, using weighted orthogonal distance regression in program Igor Pro. A comparison of  $\delta^{50}\text{Ti}$  vs.  $\delta^{46}\text{Ti}$  with theoretical fractionation lines is shown in Fig. 6b. Here 95% confidence envelopes are too narrow to be visible. (For interpretation of the references to colour in this figure legend, the reader is referred to the web version of this article.)

slopes are the exponent values  $\beta$  in the three-isotope relationships given by Eq. (8). For comparison,  $\beta$  values were calculated for different fractionation laws using Eq. (9), where  $m$  is the molar mass of species Ca or  $\text{TiO}_2$ . Here we take the relationships of  $\delta^{44}\text{Ca}$  vs.  $\delta^{42}\text{Ca}$  and of  $\delta^{50}\text{Ti}$  vs.  $\delta^{48}\text{Ti}$  as examples. In the relationship of  $\delta^{44}\text{Ca}$ – $\delta^{42}\text{Ca}$ , the theoretical  $\beta_{\text{Ca}}$  values are 1.91 (equilibrium law), 1.95 (exponential law), 1.93 (Rayleigh law), and 2.00 (power law), while in the relationship of  $\delta^{50}\text{Ti}$  vs.  $\delta^{48}\text{Ti}$ ,  $\beta_{\text{TiO}_2}$  values are  $-2.85$  (equilibrium law),  $-2.92$  (exponential law),  $-2.89$  (Rayleigh law), and  $-3.00$  (power law). The results show that the exponent values calculated with the Rayleigh fractionation law ( $\beta_{\text{Ca}} = 1.93$  and  $\beta_{\text{TiO}_2} = -2.89$ ) agree with the values found experimentally ( $\beta_{\text{Ca}} = 1.93 \pm 0.01$  and  $\beta_{\text{TiO}_2} = -2.88 \pm 0.02$ ). Thus, the MDFs of Ca and  $\text{TiO}_2$  follow the Rayleigh law. This observation can be seen clearly in Fig. 6, where the deviations from the Rayleigh law are plotted vs.  $\delta^{42}\text{Ca}$  (Fig. 6a) and vs.  $\delta^{48}\text{Ti}$  (Fig. 6b) for the experimental data and for other laws. Experimental MDFs follow the Rayleigh law. Note that fractionations of other titanium isotopes also follow the Rayleigh law (not shown here). For the widely used calcium anomaly indicator  $^{48}\text{Ca}$ , its MDF composition was not measured, because  $^{43}\text{Ca}$ – $^{48}\text{Ca}$  was used as a double spike in the measurements. However, we expect that the relationships of  $\delta^{48}\text{Ca}$  vs.

$\delta^{42}\text{Ca}$  and of  $\delta^{43}\text{Ca}$  vs.  $\delta^{42}\text{Ca}$  follow the Rayleigh law, as found for  $\delta^{44}\text{Ca}$  vs.  $\delta^{42}\text{Ca}$  and all titanium isotopes.

#### 5.4. Correction for mass-dependent fractionation (MDF) in isotope anomaly measurements

The Rayleigh MDF law we determined for Ca and  $\text{TiO}_2$  have an important application in the study of isotope anomalies in early Solar System materials. An isotope anomaly is defined as the isotope enrichment or depletion relative to terrestrial composition after correcting for the instrumental and natural MDFs using the appropriate MDF laws. Instrumental MDFs are best described by the exponential law (Russell et al., 1978; Maréchal et al., 1999), but MDF laws for evaporation, the process most likely to have produced significant MDF effects in CAIs and chondrules, have only been quantified for magnesium prior to this study (Davis et al., 2005). The common practice to correct for natural MDFs in isotope anomaly measurements is based on two assumptions: (1) an exponential law is applicable and (2) pure atoms rather than molecules are used as species (*i.e.*, Ti atoms, not  $\text{TiO}_2$  molecules). However, if the true MDF law is different from the exponential law, and if the true species is a molecule, not an atom, the two assumptions could cause inappropriate MDF corrections and thus could introduce artificial isotope anomalies (Tang and Dauphas, 2012). Therefore, future isotope anomaly studies should take into considerations the following two findings from our evaporation experiments: (1) calcium and titanium isotope fractionations produced by free evaporation into a vacuum follow the Rayleigh MDF law, not the exponential law; and (2)  $\text{TiO}_2$  molecules rather than Ti atoms appears to be the dominant evaporating species in our experiments. There is a complication: equilibrium thermodynamic calculations at temperatures and pressures appropriate for the solar nebula (*e.g.*,  $P_{\text{tot}} = 10^{-3}$  atm,  $T = 1680$  K, gas of solar composition) show that the speciation of gas-phase titanium is different:  $\sim 80\%$   $\text{TiO}$ ,  $\sim 20\%$   $\text{TiO}_2$  (L. Grossman, pers. comm.). This occurs because solar nebular gases are much more reducing than the gas above the samples in our experiments, and partial pressures of titanium-bearing species are lower. Thus, the MDF law appropriate for CAI evaporation depends on the conditions under which evaporation occurred, which is not well known. This is another source of uncertainty in correcting for MDF effects and searching for MIF effects.

No apparent artificial titanium isotope anomaly has been found in evaporation samples from our experiments, if we use the two incorrect assumptions (an exponential MDF law and titanium atoms as the dominant species) to correct for the titanium MDFs (*i.e.*,  $\epsilon^{50}\text{Ti}$  in Fig. 7). We found that the direct measurements of  $\epsilon^{50}\text{Ti}$  after correcting for titanium MDFs by assuming an exponential law for titanium atoms in evaporation samples happen to lie on the Rayleigh fractionation line for  $\text{TiO}_2$  species (Fig. 7a). So if we took the incorrect evaporating species Ti atom and assume all possible laws for the correction, we found the direct measurements after making the common correction lie on the exponential fractionation line for titanium

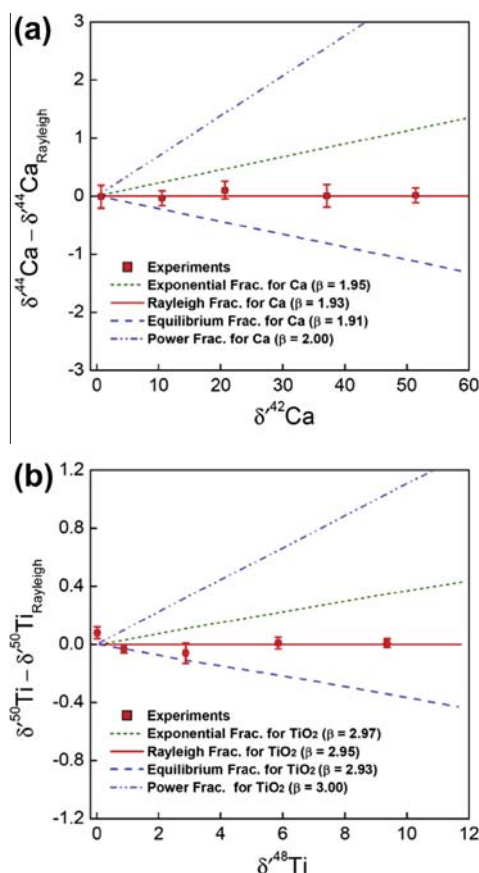


Fig. 6. The deviations from the Rayleigh law are plotted vs.  $\delta^{42}\text{Ca}$  (a) and vs.  $\delta^{48}\text{Ti}$  (b) for the experimental data (red squares) and for exponential law, equilibrium law, and power law.



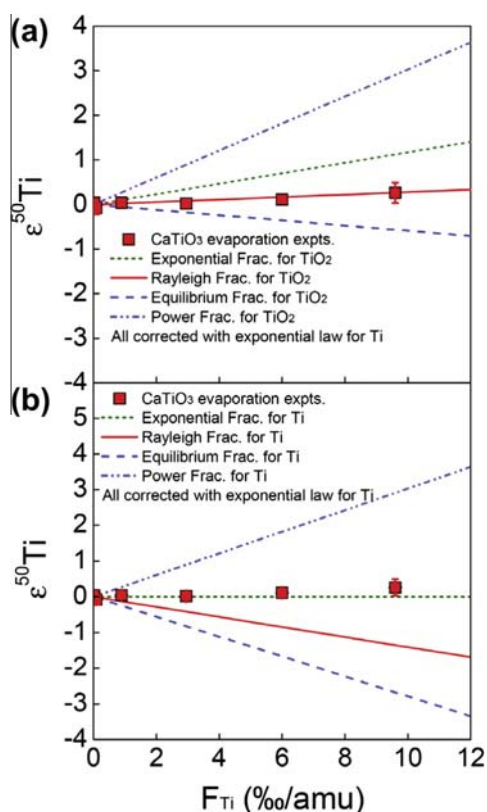


Fig. 7. No apparent artificial isotope anomalies  $\epsilon^{50}\text{Ti}$  (red squares) introduced by assuming the exponential fractionation law for Ti atom. Two separate steps generated all the lines in both panels: fractionation and correction (also see Eq. A13 of Tang and Dauphas, 2012). (a) We first calculated the titanium mass-dependent fractionation following all possible laws for  $\text{TiO}_2$ . Then, we followed the common practice (*i.e.*, assuming an exponential law for Ti atom) to correct for titanium mass-dependent fractionation. The data from direct measurements (red squares) were also corrected for titanium mass-dependent fractionation following the common practice, and they lie on the red line. It indicates that the titanium mass-dependent fractionation resulted from the Rayleigh law for  $\text{TiO}_2$  (red line) can be coincidentally corrected by using an exponential law for Ti atom. (b) The lines were generated in a similar way as those in Fig. 8a, with the only difference that now Ti atom was used as the evaporating species instead of  $\text{TiO}_2$ . (For interpretation of the references to colour in this figure legend, the reader is referred to the web version of this article.)

species (Fig. 7b). It indicates that the two incorrect assumptions in common practice coincidentally compensate for each other (see Eq. A13 of Tang and Dauphas, 2012). Therefore previously published data of titanium isotope anomalies happen to be correct, even for samples with significantly high titanium MDF due to evaporation processes. However, if the fractionation took place under reducing, solar nebular conditions, the evaporating species could be predominantly TiO and for the range of  $\delta^{49}\text{Ti}$  values seen in normal CAIs ( $-2.7$  to  $+4.0$ ; Zhang et al., 2012b), would produce shifts in  $\epsilon^{50}\text{Ti}$  of 0.2 relative to a Rayleigh law with  $\text{TiO}_2$ , comparable to typical measurement uncertainties.

However, taking Ca atoms as the evaporating species and assuming the exponential law to correct the MDF for

calcium, we found that this commonly used practice would induce an artificial calcium isotope anomaly in our evaporate residues (*i.e.*,  $\epsilon^{40}\text{Ca}$ ) (Fig. 8). The artificial calcium isotope anomaly as a function of  $F_{\text{Ca}}$  lies on the Rayleigh

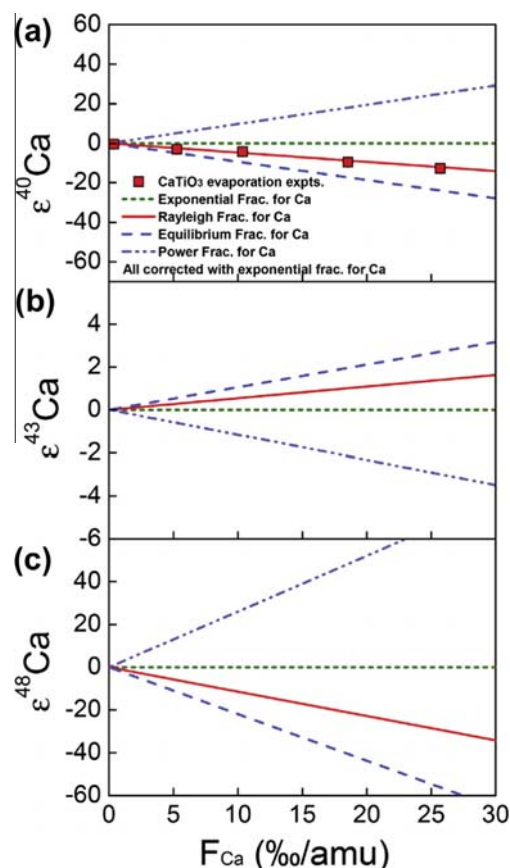


Fig. 8. Artificial calcium isotope anomalies  $\epsilon^{40}\text{Ca}$  (a),  $\epsilon^{43}\text{Ca}$  (b), and  $\epsilon^{48}\text{Ca}$  (c) introduced by assuming exponential fractionation law for Ca species. Two separate steps generated all the lines: fractionation and correction (also see Eq. A13 of Tang and Dauphas, 2012). We first calculated the calcium mass-dependent fractionation following all possible laws for Ca atom. Then, we followed the common practice (*i.e.*, assuming an exponential law for Ca atom) to correct for calcium mass-dependent fractionation. The  $\epsilon^{40}\text{Ca}$  data from direct measurements [red squares on panel (a)] were also corrected for calcium mass-dependent fractionation following the common practice, and they lie on the red line on panel (a).  $\epsilon^{43}\text{Ca}$  and  $\epsilon^{48}\text{Ca}$  were not measured because  $^{43}\text{Ca}$ – $^{48}\text{Ca}$  was used as a double spike, but their artificial anomalies are expected to lie on the Rayleigh fractionation line. The artificial  $^{43}\text{Ca}$  and  $^{48}\text{Ca}$  anomalies could, in principle, affect our calcium isotopic measurements because we used the calcium isotopic composition of NIST SRM 915a as the unspiked measurement in the  $^{43}\text{Ca}$ – $^{48}\text{Ca}$  double spike calculation. However, over 95 % of  $^{48}\text{Ca}$  and  $^{43}\text{Ca}$  in the spiked sample come from the  $^{43}\text{Ca}$ – $^{48}\text{Ca}$  double spike, the errors in  $\delta^{\text{Ca}}$  introduced by using NIST SRM 915a composition as the unspiked measurement are comparable to their analytical uncertainties. For example, this approach introduces errors of 0.09 and 0.05 in the reported  $\delta^{44}\text{Ca}$  and  $\delta^{42}\text{Ca}$ , respectively, for the most fractionated sample CT-200. (For interpretation of the references to colour in this figure legend, the reader is referred to the web version of this article.)

fractionation line, with artificial  $\epsilon^{40}\text{Ca}$  deficits as much as  $-4.7\text{‰}$  when  $F_{\text{Ca}}$  is about 10‰ per amu (Fig. 8a). This is confirmed by the direct measurement of  $\epsilon^{40}\text{Ca}$ . Since we did not measure artificial anomalies in  $^{43}\text{Ca}$  and  $^{48}\text{Ca}$  directly (because these isotopes were used in the double spike), predicted artificial isotope anomalies for these isotopes were also plotted in Fig. 8b and c, respectively, with slight  $\epsilon^{43}\text{Ca}$  excesses of 0.54‰ and large  $\epsilon^{48}\text{Ca}$  deficits of  $-11.4\text{‰}$  at  $F_{\text{Ca}}$  around 10‰ per amu. These results reveal that the common practice of using the exponential law assumption for correcting calcium MDF could introduce spurious anomalies, if calcium isotopes fractionation follows the Rayleigh law during high temperature evaporation (e.g., Ireland et al., 1992).

It is unclear at this stage whether the results of our evaporation experiments can be directly applied to natural materials, such as CAIs. For example, Ireland et al. (1992) documented large Ti isotope fractionations, up to 20‰ per amu, in HAL-type hibonites from refractory inclusions. The negative  $F_{\text{Ti}}$  vs.  $\text{TiO}_2$  abundance trend led them to argue that the evaporating species must have a mass of 140 amu, much heavier than  $\text{TiO}_2$  (see their Fig. 9). Clearly, experiments with starting compositions and evaporating conditions similar to those that generated CAIs are required for a better understanding of the origin of CAIs.

## 6. CONCLUSIONS

In this study we have investigated the fundamental properties of mass-dependent isotopic fractionations of two highly refractory elements, calcium and titanium, during high temperature evaporation of synthetic perovskite ( $\text{CaTiO}_3$ ). We found that molten  $\text{CaTiO}_3$  evaporated incongruently, with Ca and  $\text{TiO}_2$  being the likely dominant evaporation species in the experiments. It was further found that both calcium and titanium evaporation MDFs follow the Rayleigh law, not the widely assumed exponential law. We also estimated the evaporation coefficients of calcium and titanium from the  $\text{CaTiO}_3$  liquid. The validity of the common practice of assuming an exponential fractionation law when making mass-dependent fractionation correction in the study of isotope anomalies was examined. We found that this assumption does not cause apparent artificial titanium isotope anomalies due to compensating errors, but can cause significant artificial calcium isotope anomalies for significantly mass-fractionated samples.

## ACKNOWLEDGMENTS

This work was supported by the National Aeronautics and Space Administration (NASA) through grants NNX11AK82G (SH and SBJ), NNX09AG39G (AMD), NNX12AH60G (ND), NSF EAR-0820807 (ND), and a Packard Fellowship (ND).

## APPENDIX A

Let us assume total evaporated vapor pressures for calcium and titanium are

$$P_{\text{tot,Ca}} = x, \quad (\text{A1})$$

$$P_{\text{tot,Ti}} = r \times x, \quad (\text{A2})$$

respectively, where  $P_{\text{tot,Ca}} = P_{\text{Ca}} + P_{\text{CaO}}$ ,  $P_{\text{tot,Ti}} = P_{\text{Ti}} + P_{\text{TiO}} + P_{\text{TiO}_2}$ , and  $r = P_{\text{tot,Ti}}/P_{\text{tot,Ca}}$ . Based on valence balance by assuming the residues are mixtures of two phases  $\text{CaTiO}_3$  and  $\text{TiO}_2$  (i.e.,  $\text{Ca}^{2+}$ ,  $\text{Ti}^{4+}$ ,  $\text{O}^{2-}$ ), we have

$$\begin{aligned} P_{\text{tot,O}} &= P_{\text{tot,Ca}} + 2P_{\text{tot,Ti}} = x + 2(r \times x) \\ &= (1 + 2r) \times x. \end{aligned} \quad (\text{A3})$$

where  $P_{\text{tot,O}} = P_{\text{O}} + 2P_{\text{O}_2} + P_{\text{CaO}} + P_{\text{TiO}} + 2P_{\text{TiO}_2}$ . Combining equations (A1), (A2), and (A3), we obtain

$$\begin{aligned} \frac{P_{\text{tot,O}}}{P_{\text{tot,Ca}} + P_{\text{tot,Ti}}} &= \frac{P_{\text{O}} + 2P_{\text{O}_2} + P_{\text{CaO}} + P_{\text{TiO}} + P_{\text{TiO}_2}}{P_{\text{Ca}} + P_{\text{CaO}} + P_{\text{Ti}} + P_{\text{TiO}} + P_{\text{TiO}_2}} \\ &= \frac{(1 + 2r) \times x}{x + r \times x} = \frac{1 + 2r}{1 + r}. \end{aligned} \quad (\text{A4})$$

Equation (A4) can be rearranged into the Eq. g in the text:

$$\begin{aligned} (1 + 2r)(P_{\text{Ca}} + P_{\text{CaO}} + P_{\text{Ti}} + P_{\text{TiO}} + P_{\text{TiO}_2}) \\ = (1 + r)(P_{\text{O}} + 2P_{\text{O}_2} + P_{\text{CaO}} + P_{\text{TiO}} + 2P_{\text{TiO}_2}). \end{aligned} \quad (\text{A5})$$

## REFERENCES

- Albarède F. and Beard B. (2004) Analytical methods for non-traditional isotopes. *Rev. Mineral. Geochem.* **55**, 113–152.
- Albarède F., Telouk P., Blichert-Toft J., Boyet M., Agranier A. and Nelson B. (2004) Precise and accurate isotopic measurements using multiple-collector ICPMS. *Geochim. Cosmochim. Acta* **68**, 2725–2744.
- Birck J. L. (2004) An overview of isotopic anomalies in extraterrestrial materials and their nucleosynthetic heritage. *Rev. Mineral. Geochem.* **55**, 25–64.
- Chase M. W. Jr. (1998) NIST-JANAF thermodynamical tables, 4th ed., *J. Phys. Chem. Ref. Data Monogr.* **9**.
- Chen H.-W., Lee T., Lee D.-C., Jiun-San Shen. J. and Chen J.-C. (2011)  $^{48}\text{Ca}$  heterogeneity in differentiated meteorites. *Astrophys. J.* **743**, L23–L27.
- Clayton R. N., Hinton R. W. and Davis A. M. (1988) Isotopic variations in the rock-forming elements in meteorites. *Philos. Trans. R. Soc. London A* **325**, 483–501.
- Daněk V. and Nerád I. (2002) Phase diagram and structure of melts of the system  $\text{CaO-TiO}_2\text{-SiO}_2$ . *Chem. Pap.* **56**, 241–246.
- Dauphas N. and Chaussidon M. (2011) A perspective from extinct radionuclides on a young stellar object: the Sun and its accretion disk. *Ann. Rev. Earth Planet. Sci.* **39**, 351–386.
- Dauphas N. and Rouxel (2006) Mass spectrometry and natural variations of iron isotopes. *Mass Spectrom. Rev.* **25**, 515–550.
- Dauphas N., Marty B. and Reisberg L. (2002) Molybdenum evidence for inherited planetary scale isotope heterogeneity of the protosolar nebula. *Astrophys. J.* **565**, 640–644.
- Dauphas N., Janney P. E., Mendybaev R. A., Wadhwa M., Richter F. M., Davis A. M., Zuilen M., Hines R. and Nicole Foley N. (2004) Chromatographic separation and multicollector-ICPMS analysis of iron. Investigating mass-dependent and -independent isotope effects. *Anal. Chem.* **76**, 5855–5863.
- Davis A. M. and McKeegan K. D. (2014) Short-lived radionuclides and early solar system chronology. In *Meteorites and Cosmochemical Processes* (ed. A. M. Davis), vol. 1 Treatise on Geochemistry, 2nd Ed. (Exec. Eds. H. D. Holland and K. K. Turekian), Elsevier, Oxford, pp. 361–395.
- Davis A. M., Hashimoto A., Clayton R. N. and Mayeda T. K. (1990) Isotope mass fractionation during evaporation of  $\text{Mg}_2\text{SiO}_4$ . *Nature* **347**, 655–658.

- Davis A. M., Hashimoto A., Clayton R. N. and Mayeda T. K. (1995) Isotopic and chemical fractionation during evaporation of  $\text{CaTiO}_3$ . *Lunar Planet. Sci.* **26**, 317–318.
- Davis A. M., Richter F. M., Mendybaev R. A., Janney P. E., Wadhwa M. and McKeegan K. D. (2005) Isotopic mass fractionation laws and the initial solar system  $^{26}\text{Al}/^{27}\text{Al}$  ratio. *Lunar Planet. Sci.* **36**, #2334.
- Esat T. M., Spear R. H. and Taylor S. R. (1986) Isotope anomalies induced in laboratory distillation. *Nature* **319**, 576–578.
- Estrade N., Carignan J., Sonke J. E. and Donard O. F. X. (2009) Mercury isotope fractionation during liquid-vapor evaporation experiments. *Geochim. Cosmochim. Acta* **73**, 2693–2711.
- Fahey A. J., Zinner E. K., Crozaz G. and Kornacki A. S. (1987) Micro distribution of Mg isotopes and REE abundances in a Type A calcium-aluminum-rich inclusion from Efremovka. *Geochim. Cosmochim. Acta* **51**, 3215–3229.
- Farkaš J., Déjeant A., Novák M. and Jacobsen S. B. (2011) Calcium isotope constraints on the uptake and sources of  $\text{Ca}^{2+}$  in a base-poor forest: a new concept of combining stable ( $\delta^{44}/^{42}\text{Ca}$ ) and radiogenic ( $\epsilon\text{Ca}$ ) signals. *Geochim. Cosmochim. Acta* **75**, 7031–7046.
- Grossman L., Ebel D. S., Simon S. B., Davis A. M., Richter F. M. and Parsad N. M. (2000) Major element chemical and isotopic compositions of refractory inclusions in C3 chondrites: the separate roles of condensation and evaporation. *Geochim. Cosmochim. Acta* **64**, 2879–2994.
- Habfast K. (1998) Fractionation correction and multiple collectors in thermal ionization isotope ratio mass spectrometry. *Int. J. Mass Spectrom.* **176**, 133–148.
- Hart S. R. and Zindler A. (1989) Isotope fractionation laws: a test using calcium. *Int. J. Mass Spectrom. Ion Proc.* **89**, 287–301.
- Hashimoto A., Holmberg B. B. and Wood J. A. (1989) Effects of melting on evaporation kinetics. *Meteoritics* **24**, 276.
- Hashimoto A. (1990) Evaporation kinetics of forsterite and implications for the early solar nebula. *Nature* **347**, 53–55.
- Hashimoto A. (1991a) Evaporation kinetics of oxides of rare earth and refractory trace elements, and the chemical fractionation of hibonite by evaporation. *Lunar Planet. Sci.* **22**, 529–530.
- Hashimoto A. (1991b) Evaporation of melilite. *Meteoritics* **26**, 344.
- Hashimoto A. (1991c) Prediction of activities of oxide components in the multicomponent liquid system  $\text{FeO-MgO-CaO-Na}_2\text{O-AlO}_{1.5}\text{-SiO}_2$ . *Lunar Planet. Sci.* **22**, 533–534.
- Hirth J. P. and Pound G. M. (1963) *Condensation and Evaporation: Nucleation and Growth Kinetics*. Pergamon, Oxford, 192 p.
- Huang S., Farkaš J. and Jacobsen S. B. (2010) Calcium isotopic fractionation between clinopyroxene and orthopyroxene from mantle peridotites. *Earth Planet. Sci. Lett.* **292**, 337–344.
- Huang S., Farkaš J. and Jacobsen S. B. (2011) Stable calcium isotopic compositions of Hawaiian shield lavas: evidence for recycling of ancient marine carbonates into the mantle. *Geochim. Cosmochim. Acta* **75**, 4987–4997.
- Huang S., Farkaš J., Yu G., Petaev M. I. and Jacobsen S. B. (2012) Calcium isotopic ratios and rare earth element abundances in refractory inclusions from the Allende CV3 chondrite. *Geochim. Cosmochim. Acta* **77**, 252–265.
- Ireland T. R. (1990) Presolar isotopic and chemical signatures in hibonite-bearing refractory inclusions from the Murchison carbonaceous chondrites. *Geochim. Cosmochim. Acta* **54**, 3219–3237.
- Ireland T. R., Zinner E. K., Fahey A. J. and Esat T. M. (1992) Evidence for distillation in the formation of HAL and related hibonite inclusions. *Geochim. Cosmochim. Acta* **56**, 2503–2520.
- Jacob K. T. and Gupta S. (2009) Phase diagram of the system  $\text{Ca-Ti-O}$  at 1200 K. *Bull. Mater. Sci.* **32**, 611–616.
- Knight K. B., Kita N. T., Mendybaev R. A., Richter F. M., Davis A. M. and Valley J. W. (2009) Silicon isotopic fractionation of CAI-like vacuum evaporation residues. *Geochim. Cosmochim. Acta* **73**, 6390–6401.
- Kuroda D. and Hashimoto A. (2002) The reaction of forsterite with hydrogen-its apparent and real temperature dependences. *Antarctic Meteor.* **15**, 152–164.
- Leya I., Schönbächler M., Krähenbühl U. and Halliday A. N. (2009) New titanium isotope data for Allende and Efremovka CAIs. *Astrophys. J.* **702**, 1118–1126.
- Leya I., Schönbächler M., Wiechert U., Krähenbühl U. and Halliday A. N. (2008) Titanium isotopes and the radial heterogeneity of the solar system. *Earth Planet. Sci. Lett.* **266**, 233–244.
- MacPherson G. J. (2014) Calcium–aluminum-rich inclusions in chondritic meteorites. In *Meteorites and Cosmochemical Processes* (ed. A. M. Davis), vol. I Treatise on Geochemistry, 2nd Ed. (Exec. Eds. H. D. Holland and K. K. Turekian), Elsevier, Oxford, pp. 139–179.
- Maréchal C. N., Télouk P. and Albarède F. (1999) Precise analysis of copper and zinc isotopic compositions by plasma-source mass spectrometry. *Chem. Geol.* **156**, 251–273.
- Molini-Velsko C., Mayeda T. K. and Clayton R. N. (1987). *Proc. Lunar Planet. Sci.* **18**, 657–658.
- Moynier F., Simon J. I., Podosek F. A., Meyer B. S., Brannon J. and DePaolo D. J. (2010) Ca isotope effects in Orgueil leachates and the implications for the carrier phases of  $^{54}\text{Cr}$  anomalies. *Astrophys. J.* **718**, L7–L13.
- Nagahara H. and Ozawa K. (1996) Evaporation of forsterite in  $\text{H}_2$  gas. *Geochim. Cosmochim. Acta* **60**, 1445–1459.
- Nichols, Jr., R. H., Grimley R. T. and Wasserburg G. J. (1998) Measurement of gas-phase species during Langmuir evaporation of forsterite. *Meteorit. Planet. Sci.* **33**, A115–A116.
- Nichols, Jr., R. H., Wasserburg G. J. and Grimley R. T. (1995) Evaporation of forsterite: identification of gas-phase species via Knudsen cell mass spectrometry. *Lunar Planet. Sci.* **26**, 1047–1048.
- Niederer F. R. and Papanastassiou D. A. (1984) Ca isotopes in refractory inclusions. *Geochim. Cosmochim. Acta* **48**, 1279–1293.
- Niederer F. R., Papanastassiou D. A. and Wasserburg G. J. (1985) Absolute isotopic abundances of Ti in meteorites. *Geochim. Cosmochim. Acta* **49**, 835–851.
- Pouchou J. L. and Pichoir F. (1984) A new model for quantitative X-ray microanalysis. Part I: application to the analysis of homogeneous samples. *Rech. Aeros.* **3**, 13–38.
- Richter F. M. (2004) Timescales determining the degree of kinetic isotope fractionation by evaporation and condensation. *Geochim. Cosmochim. Acta* **68**, 4971–4992.
- Richter F. M., Davis A. M., Ebel D. S. and Hashimoto A. (2002) Elemental and isotopic fractionation of Type B CAIs: experiments, theoretical considerations, and constraints on their thermal evolution. *Geochim. Cosmochim. Acta* **66**, 521–540.
- Richter F. M., Janney P. E., Mendybaev R. A., Davis A. M. and Wadhwa M. (2007) Elemental and isotopic fractionation of Type B CAI-like liquids by evaporation. *Geochim. Cosmochim. Acta* **71**, 5544–5564.
- Richter F. M., Mendybaev R. A., Christensen J. N., Ebel D. and Gaffney A. (2011) Laboratory experiments bearing on the origin and evolution of olivine-rich chondrules. *Meteorit. Planet. Sci.* **46**, 1152–1178.
- Robie R. A., Hemingway B. S. and Fisher J. R. (1979) Thermodynamic properties of minerals and related substance at 298.15 K and 1 Bar ( $10^5$  Pascals) pressure and at higher temperatures. *Geol. Survey Bull.* **1452**, 456.
- Russell W. A., Papanastassiou D. A. and Tombrello T. A. (1978) Ca isotope fractionation on the Earth and other solar system materials. *Geochim. Cosmochim. Acta* **42**, 1075–1090.

- Sata T., Sasamoto T., Lee H. L. and Maeda E. (1978) Vaporization processes from magnesium materials. *Rev. Int. Hautes Temp. Refract.* **15**, 237–248.
- Schönbachler M., Rehkamper M., Lee D. C. and Halliday A. N. (2004) Ion exchange chromatography and high precision isotopic measurements of zirconium by MC-ICP-MS. *Analyst* **129**, 32–37.
- Shornikov S. I. (2011) A thermodynamic investigation of evaporation of oxide melts containing titanium dioxide. *Vestnik Otdelenia nauk o Zemle RAN* **3**, NZ6101.
- Shornikov S. I. and Archakov I. Y. (2003) Mass spectrometric study of thermodynamic properties of the  $\text{SiO}_2$ - $\text{CaTiO}_3$  melts. *Proc. II Intern. Symp. High Temp. Mass Spectrom.*, 112–116.
- Simon J. I., DePaolo D. J. and Moynier F. (2009) Calcium isotope composition of meteorites, Earth, and Mars. *Astrophys. J.* **702**, 707–715.
- Somorjai G. A. and Lester J. E. (1967) Evaporation mechanism of solids. *Prog. Solid State Chem.* **4**, (ed. Reiss H.), 1–52.
- Tachibana S., Nagahara H., Ozawa K. and Yamada M. (2007) Isotopic fractionation of iron during kinetic evaporation of metallic iron. *Meteorit. Planet. Sci.* **42**, #5328T.
- Tachibana S., Nagahara H., Ozawa K., Ikeda Y., Nomura R., Tatsumi K. and Joh Y. (2011) Kinetic condensation and evaporation of metallic iron and implications for metallic iron dust formation. *Astrophys. J.* **736**, 1–8.
- Takigawa A., Tachibana S., Nagahara H., Ozawa K. and Yokoyama M. (2009) Anisotropic evaporation of forsterite and its implication for dust formation conditions in circumstellar environments. *Astrophys. J.* **707**, L97–L101.
- Tang H. and Dauphas N. (2012) Abundance, distribution, and origin of  $^{60}\text{Fe}$  in the solar protoplanetary disk. *Earth Planet. Sci. Lett.* **359**, 248–263.
- Trinquier A., Elliott T., Ulfbeck D., Coath C., Krot A. N. and Bizzarro M. (2009) Origin of nucleosynthetic isotope heterogeneity in the solar protoplanetary disk. *Science* **324**, 374–376.
- Tsuchiyama A., Takahashi T. and Tachibana S. (1998) Evaporation rates of forsterite in the system  $\text{Mg}_2\text{SiO}_4$ - $\text{H}_2$ . *Mineral. J.* **20**, 113–126.
- Wang J. H., Davis A. M., Clayton R. N. and Hashimoto A. (1999) Evaporation of single crystal forsterite: evaporation kinetics, magnesium isotope fractionation, and implications of mass-dependent isotopic fractionation of a diffusion-controlled reservoir. *Geochim. Cosmochim. Acta* **63**, 953–966.
- Wang J. H., Davis A. M., Clayton R. N. and Mayeda T. K. (1994) Kinetic isotope fractionation during the evaporation of the iron oxide from liquid state. *Lunar Planet. Sci.* **25**, 1459–1460.
- Wang J., Davis A. M., Clayton R. N., Mayeda T. K. and Hashimoto A. (2001) Chemical and isotopic fractionation during the evaporation of the  $\text{FeO}$ - $\text{MgO}$ - $\text{SiO}_2$ - $\text{CaO}$ - $\text{Al}_2\text{O}_3$ - $\text{TiO}_2$  rare earth element melt system. *Geochim. Cosmochim. Acta* **65**, 479–494.
- Wombacher F., Rehkäper M. and Mezger K. (2004) Determination of the mass-dependence of cadmium isotope fractionation during evaporation. *Geochim. Cosmochim. Acta* **68**, 2349–2357.
- Yamada M., Tachibana S., Nagahara H. and Ozawa K. (2006) Anisotropy of Mg isotopic fractionation during evaporation and Mg self-diffusion of forsterite in vacuum. *Planet. Space Sci.* **54**, 1096–1106.
- Young E. D. and Galy A. (2004) The isotope geochemistry and cosmochemistry of magnesium. *Rev. Mineral Geochem.* **55**, 197–230.
- Young E. D., Galy A. and Nagahara H. (2002) Kinetic and equilibrium mass-dependent isotope fractionation laws in nature and their geochemical and cosmochemical significance. *Geochim. Cosmochim. Acta* **66**, 1095–1104.
- Yu Y., Hewins R. H., Alexander C. M. O'D. and Wang J. (2003) Experimental study of evaporation and isotopic mass fractionation of potassium in silicate melts. *Geochim. Cosmochim. Acta* **67**, 773–786.
- Zhang J., Dauphas N., Davis A. M. and Pourmand A. (2011) A new method for MC-ICPMS measurement of titanium isotopic composition: identification of correlated isotope anomalies in meteorites. *J. Anal. At. Spectrom.* **26**, 2197–2205.
- Zhang J., Dauphas N., Davis A. M., Leya I. and Fedkin A. (2012a) The proto-Earth as a significant source of lunar material. *Nature Geosci.* **5**, 251–255.
- Zhang J., Davis A. M. and Dauphas N. (2012b) Titanium isotopic compositions in calcium-aluminum-rich inclusions. *Meteorit. Planet. Sci.* **47**, #5286.

Associate editor: Qing-Zhu Yin